

Selection rules for the excitation of quantum dots by spatially structured light beams: Application to the reconstruction of higher excited exciton wave functions

M. Holtkemper,¹ G. F. Quinteiro², D. E. Reiter¹ and T. Kuhn¹

¹*Institut für Festkörperteorie, Universität Münster, Wilhelm-Klemm-Straße 10, 48149 Münster, Germany*

²*MIT and Departamento de Física, Universidad Nacional del Nordeste, Campus Deodoro Roca, Corrientes, Argentina*

 (Received 22 April 2020; revised 21 August 2020; accepted 1 October 2020; published 30 October 2020)

Spatially structured light fields applied to semiconductor quantum dots yield fundamentally different absorption spectra than homogeneous beams. In this paper, we provide a detailed theoretical discussion of the resulting spectra for different light beams using a cylindrical multipole expansion. For the description of the quantum dots we employ a model based on the envelope function approximation including Coulomb interaction and valence band mixing. The combination of a single spatially structured light beam and state mixing allows all exciton states in the quantum dot to become optically addressable. Furthermore, we demonstrate that the beams can be tailored such that single states are selectively excited, without the need of spectral separation. Using this selectivity, we propose a method to measure the exciton wave function of the quantum dot eigenstate. The measurement goes beyond electron density measurements by revealing the spatial phase information of the exciton wave function. Such an extraction of phase information is known from polarization-sensitive measurements; however, here the infinitely large spatial degree of freedom can be accessed by the beam profile in addition to the two-dimensional polarization degree of freedom.

DOI: [10.1103/PhysRevB.102.165315](https://doi.org/10.1103/PhysRevB.102.165315)

I. INTRODUCTION

Spatially structured light (SSL) fields feature strong gradients in the light intensity, in contrast to standard Gaussian beams which can often be approximated by plane waves. SSL appears in near-field setups [1], waveguides [2], photonic crystals [3], or other cavities [4–6], as well as in the far field of freely propagating beams [7–10], denoted, e.g., as Hermite-Gaussian, Laguerre-Gaussian, or Bessel beams. The spatial structure of such fields provides several interesting features: First, it is possible to get around the diffraction limit [11,12]. Second, the infinite degree of freedom defined for instance by the orbital angular momentum of the beam provides a much more powerful approach to carry (quantum) information than the two-dimensional polarization [8,13,14], thereby enabling hyperentanglement [13,15,16], state cloning [17], and highly increased data transfer rates in optical communication [18–20].

Here we study theoretically the interaction of SSL with a single self-assembled semiconductor quantum dot (QD). QDs provide a quantized and widely adjustable electronic level structure and are established components in many modern applications [21–26], especially in the context of quantum information technology [27–30]. In addition to the energetically lowest four levels, i.e., the ground state bright and dark excitons, which play a central role for many applications, also higher excited states become interesting. The latter can be used, e.g., to describe metastable states in charged QDs [31], to create and describe multiexciton states [32–40], for state preparation schemes [41,42], to study dephasing and relaxation processes [31,43,44], or for resonant absorption within

a QD [43,45–48]. To utilize higher excited electronic states, they need to be addressable, selectively excitable, and identifiable. In this paper, we will show that these three prerequisites are highly improved when using SSL.

(1) *Addressability.* Plane wave selection rules enable only specific electronic transitions. The number of addressable states is highly increased when using SSL with their corresponding multipole transitions [49–51]. However, several electronic states stay unaddressable within simplified QD models. We show within a realistic QD model including Coulomb interactions and valence band mixing that each eigenstate becomes accessible by an appropriate SSL field. The oscillator strength of these previously dark states varies from negligible to strong, depending on the individual state mixtures. We discuss relevant coupling mechanisms and the influence of symmetry breaking. The oscillator strengths are visualized within calculated absorption spectra.

(2) *Selectivity.* The QD's eigenstates are often energetically close and not individually addressable by short and thus broadband laser pulses. This limits for instance the temporal resolution in pump-probe experiments utilizing higher excited states [31]. One known way around this limit is a polarization-sensitive excitation, where even energetically arbitrarily close states (like the horizontally and vertically polarized exciton ground states) can be addressed selectively. However, the polarization sensitive excitation is limited to the two-dimensional spin degree of freedom. With our scheme we show that using the infinite spatial degree of freedom of SSL in addition to the polarization, one can highly increase the possibilities of selective excitation.

TABLE I. Definition of the basis functions used to describe the Bloch part of the wave function, corresponding parities in the x , y , and z directions (e and o denoting even and odd parity, respectively), and corresponding dipole moments.

State	ϵ_x	ϵ_y	ϵ_z	ϵ_0	$\epsilon_{\bar{x}}$	$\epsilon_{\bar{y}}$	$\epsilon_{\bar{z}}$	$\epsilon_{\bar{0}}$
Spin configuration	$\frac{1}{\sqrt{2}}(\uparrow\downarrow - \downarrow\uparrow)$	$\frac{-i}{\sqrt{2}}(\uparrow\downarrow + \downarrow\uparrow)$	$\frac{1}{\sqrt{2}}(\uparrow\uparrow + \downarrow\downarrow)$	$\frac{i}{\sqrt{2}}(\uparrow\uparrow - \downarrow\downarrow)$	$\frac{1}{\sqrt{2}}(\uparrow\uparrow - \downarrow\downarrow)$	$\frac{-i}{\sqrt{2}}(\uparrow\uparrow + \downarrow\downarrow)$	$\frac{1}{\sqrt{2}}(\uparrow\downarrow + \downarrow\uparrow)$	$\frac{i}{\sqrt{2}}(\uparrow\downarrow - \downarrow\uparrow)$
Parity (P^x, P^y, P^z)	(o,e,e)	(e,o,e)	(e,e,o)	(o,o,o)	(o,e,e)	(e,o,e)	(e,e,o)	(o,o,o)
Dipole moment $\frac{\mu}{\mu_0}$	e_x	e_y	0	0	$\sqrt{\frac{1}{3}}e_x$	$\sqrt{\frac{1}{3}}e_y$	$\sqrt{\frac{4}{3}}e_z$	0

(3) *Identification.* To identify an electronic eigenstate within a QD, one has to measure its wave function. The measurement of electron densities in QDs is possible, e.g., by scanning tunneling [52] or magnetotunneling spectroscopy [53]. We propose a method to reconstruct the wave function of excitons from pure optical experiments. Our method goes beyond today's measurements, since not just electronic densities are measurable, but the wave function itself (of course except for a global phase). Our proposed method is not restricted by the diffraction limit.

The paper is structured as follows: The models for the QD and the light-matter interaction are given in Sec. II. Analytical selection rules and absorption spectra are first presented for a simplified QD model in Sec. III and are then generalized to our full model in Sec. IV. A proposal to measure the wave functions of the QD's eigenstates is given in Sec. V. Section VI discusses the experimental viability of the considered light modes. Concluding statements are given in Sec. VII. Finally, Appendices A–F provide some background information and additional details.

II. MODEL

A. QD model

We model the electronic level structure of a QD based on the envelope function approximation. In this approach, the single-particle wave functions

$$\Psi_{a,b}(\mathbf{r}) = \sqrt{V_{\text{uc}}} \Phi_{a,b}(\mathbf{r}) u_b(\mathbf{r}) \quad (1)$$

are separated into an envelope $\Phi_{a,b}$ and a Bloch function u_b , with V_{uc} denoting the volume of the unit cell.

The Bloch part u_b is described by the Γ -point states of the underlying crystal numbered by the band index b . Here we restrict our consideration to the heavy hole (HH), light hole (LH), and lowest conduction (EL) bands, referred to by their (pseudo)spins $\pm\frac{3}{2}$ (or $\uparrow\uparrow$ and $\downarrow\downarrow$), $\pm\frac{1}{2}$ (\uparrow and \downarrow), and $\pm\frac{1}{2}$ (\uparrow and \downarrow), respectively. We use the z axis (which is the growth direction of the QD) as the quantization axis. For excitons, we get eight possible combinations of the spin states. Since we assume (as is realistic) a broken cylindrical symmetry of the QD, the most convenient basis is defined by the linearly polarized HH exciton states $\epsilon_x, \epsilon_y, \epsilon_z$, and ϵ_0 , as well as the LH exciton states $\epsilon_{\bar{x}}, \epsilon_{\bar{y}}, \epsilon_{\bar{z}}$, and $\epsilon_{\bar{0}}$, which are listed in Table I. We use a phase convention as in Ref. [48].

The envelope functions are expanded in terms of Cartesian Hermite-Gaussian functions $\Phi_{a,b}(\mathbf{r}) =$

$\tilde{\Phi}_{a^x,b}(x)\tilde{\Phi}_{a^y,b}(y)\tilde{\Phi}_{a^z,b}(z)$ with quantum numbers $\mathbf{a} = (a^x, a^y, a^z)$. States with $a^x + a^y + a^z = 0, 1, 2, \dots$ will be called s, p, d, \dots like states. LH states are labeled by capital letters S, P, D, \dots . If necessary, indices provide a distinction between a^x, a^y , and a^z , e.g., d_{xy} for $\mathbf{a} = (1, 1, 0)$. Since excitations in different in-plane directions are often similar, we use “inpl” as a label for any in-plane direction; thus for example d_{inpl} is a shortcut for d_{xx}, d_{xy} , and d_{yy} states. Transitions as well as the associated exciton states are labeled in the scheme hole \rightarrow electron.

A full configuration interaction (CI) approach is used to account for correlation effects. The CI basis states are given by electron-hole product states and the resulting exciton states are given by

$$|\Psi_X\rangle = \sum_{a_e, b_e; a_h, b_h} c_{a_e, b_e; a_h, b_h} |\Psi_{a_e, b_e}\rangle \otimes |\Psi_{a_h, b_h}\rangle. \quad (2)$$

Indices e (h) indicate that the summation runs only over the conduction (valence) bands. Our QD Hamiltonian reads

$$\hat{H}_{\text{QD}} = \hat{H}_{\text{EMA}} + \hat{H}_{\text{CDI}} + \hat{H}_{\text{SRE}} + \hat{H}_{\text{VBM}}$$

and includes the QD confinement within an effective mass approximation (EMA), the Coulomb direct (CDI) and short-range exchange (SRE) interactions, as well as valence band mixing (VBM) via the off-diagonal elements of a four-band Luttinger model. As an approximation to the QD confinement, we use an anisotropic harmonic potential treated in Cartesian coordinates. The frequencies of the potential $\omega_{b,\alpha} = \frac{4\hbar}{m_{b,\alpha}\beta_0^2 L_\alpha^2}$ (b denoting the band index, α the direction) are chosen such that the probability density of the ground state is reduced to $\frac{1}{e}$ at the distance $\pm\frac{1}{2}L_\alpha$ from the QD center. The QD diameters L_α are fixed to $5.8 \times 5.0 \times 2.0 \text{ nm}^3$, representing the flat geometry with slightly broken cylindrical symmetry of a typical self-assembled QD. The wave functions of the holes are assumed to be broader than those of the electrons by a factor $\beta_{\text{HH/LH}} = \beta = 1.15$ (we set $\beta_{\text{EL}} = 1.0$). We use the material parameters of CdSe [54,55], with a band gap of 1840 meV and effective masses $m_{b,\alpha}$ (in terms of the free-space electron mass m_0): $m_{\text{EL}} = 0.13m_0$, $m_{\text{HH},x/y} \approx 0.38m_0$, $m_{\text{HH},z} = m_0$, $m_{\text{LH},x/y} \approx 0.65m_0$, and $m_{\text{LH},z} \approx 0.31m_0$, deduced from the Luttinger parameters $\gamma_1 = 2.1$, $\gamma_2 = \gamma_3 = 0.55$. For the CDI, we use the static dielectric constant of bulk CdSe [55] of $\epsilon_r = 9.2$. The parameter for the coupling strength of the SRE is set to $M_{\text{SRE}} = 1.47 \text{ meV}$ by fitting experimental data from Ref. [31]. Further details of the model are discussed in Ref. [48].

B. Light-matter interaction

The light-matter interaction can be described in different gauges. The so-called twisted-light gauge [9] is highly adapted to describe the interaction of higher multipole modes with matter. However, the use of the twisted-light gauge in conjunction with the envelope function approximation is theoretically challenging and requires a reexamination of the typical approximations involved in deriving the envelope function approximation and its correspondence with the approximations made on the vector and scalar potential. Such an analysis is out of the scope of the present article, and thus we will here make use of the standard minimal-coupling Hamiltonian in Coulomb gauge to calculate the transition matrix elements. Accordingly, neglecting quadratic terms in the fields, we consider

$$\hat{H}_\gamma(t) = \frac{e}{m_0} \mathbf{A}(\mathbf{r}, t) \cdot \hat{\mathbf{p}} \quad (3)$$

with the elementary charge e , the vector potential \mathbf{A} , and the canonical momentum operator $\hat{\mathbf{p}}$. Assuming a monochromatic light field $\mathbf{A}(\mathbf{r}, t) = \tilde{\mathbf{A}}(\mathbf{r})e^{-i\omega t} + \text{c.c.}$ with the complex spatial light mode $\tilde{\mathbf{A}}(\mathbf{r})$ and the light frequency ω and using Fermi's golden rule the SSL-induced transition rate w_X from the empty QD $|0\rangle$ into an exciton state $|\Psi_X\rangle$ with energy E_X is given by

$$w_X(\omega) = \frac{2\pi}{\hbar} |\langle \Psi_X | \frac{e}{m_0} \tilde{\mathbf{A}}(\mathbf{r}) \cdot \hat{\mathbf{p}} | 0 \rangle|^2 \delta(E_X - \hbar\omega). \quad (4)$$

Such excitation rates for single QDs are measured typically by photoluminescence excitation (PLE) spectroscopy [31,47,56–58]. Since the generation of an exciton is associated with the absorption of a photon with the corresponding energy $\hbar\omega$, these PLE spectra are usually referred to as absorption spectra. Here, we will follow this terminology and use the term absorption spectra. In the plots each absorption line will be widened by a Lorentzian function with a full width at half maximum of 0.1 meV to improve visibility.

The matrix elements can be approximated by using the typical steps of the envelope function approximation: After the separation of the wave function into envelope and Bloch parts [see Eq. (1)], the transformation $\mathbf{r} \rightarrow \mathbf{r}' + \mathbf{R}$ with the position of the actual unit cell \mathbf{R} and the relative position within this unit cell \mathbf{r}' is applied. This is accompanied by $V_{\text{uc}} \sum_{\mathbf{R}} \int d^3r' \rightarrow \int d^3R \int d^3r'$ and $\Phi_{a,b}(\mathbf{r}) = \Phi_{a,b}(\mathbf{R} + \mathbf{r}') \approx \Phi_{a,b}(\mathbf{R})$. Furthermore we use the approximation that the field varies slowly over a single unit cell; thus we neglect in

$$\tilde{\mathbf{A}}(\mathbf{R} + \mathbf{r}') \cdot \hat{\mathbf{p}} = \tilde{\mathbf{A}}(\mathbf{R}) \cdot \hat{\mathbf{p}} + \sum_{\alpha \in \{x,y,z\}} \partial_{R_\alpha} \tilde{\mathbf{A}}(\mathbf{R}) \cdot r_\alpha \hat{\mathbf{p}} + \dots \quad (5)$$

all but the zeroth-order term. Since $\hat{\mathbf{p}}$ results in dipole moments on the atomic length scale of the Bloch functions (see Appendix A), higher order terms like $r_\alpha \hat{\mathbf{p}}$ would result in higher multipole transitions on the atomic scale, which can be neglected safely [59]. However, with the full dependency of $\tilde{\mathbf{A}}(\mathbf{R})$ on \mathbf{R} , all higher multipole transitions on the mesoscopic scale of the envelopes are still included. In total we

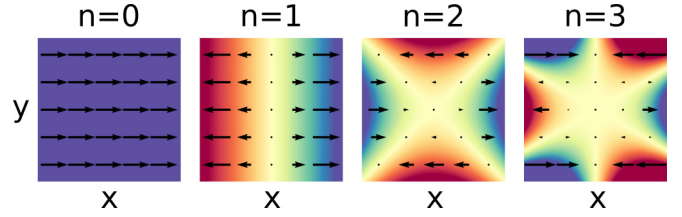


FIG. 1. Beam profiles in the QD region as described in Eq. (7) for $\theta = 0$, $\alpha = x$, and $n \in \{0, 1, 2, 3\}$. Red/blue areas symbolize opposing orientations of the field.

get

$$\begin{aligned} & \langle \Psi_{a_e, b_e} | \hat{H}_\gamma | \Psi_{a_h, b_h} \rangle \\ &= V_{\text{uc}} \int d^3r \Phi_{a_e, b_e}^*(\mathbf{r}) u_{b_e}^*(\mathbf{r}) \left[\frac{e}{m_0} \tilde{\mathbf{A}}(\mathbf{r}) \cdot \hat{\mathbf{p}} \right] \Phi_{a_h, b_h}(\mathbf{r}) u_{b_h}(\mathbf{r}) \\ &\approx \underbrace{\int d^3R \Phi_{a_e, b_e}^*(\mathbf{R}) \tilde{\mathbf{A}}(\mathbf{R}) \Phi_{a_h, b_h}(\mathbf{R})}_{M_{a_e, a_h; b_e, b_h}(\tilde{\mathbf{A}})} \cdot \underbrace{\int_{V_{\text{uc}}} d^3r' u_{b_e}^*(\mathbf{r}') \left[\frac{e \hat{\mathbf{p}}'}{m_0} \right] u_{b_h}(\mathbf{r}')}_{\mu_{b_e, b_h}}. \quad (6) \end{aligned}$$

The microscopic dipole moments μ_{b_e, b_h} for the eight basis states are known [60] up to a constant factor μ_0 . They are listed in Table I.

The focus of this work is on the evaluation of the mesoscopic transition matrix elements $M_{a_e, a_h; b_e, b_h}(\tilde{\mathbf{A}})$ for specific light fields. They depend on the spatial structure of the light field, which can be arbitrarily complicated. Typically, this problem is fixed by a spherical multipole expansion of the light fields, such that selection rules can be given in a compact form. However, we are interested in the interaction with spatially structured beams; their cylindrical geometry can be used more directly within a cylindrical multipole expansion instead of the spherical one. In the cylindrical multipole expansion the radial dependency of an arbitrary beam profile is described by Bessel functions $J_n(q_r r)$ and the angular dependency either by the real functions $\cos(n\varphi)$ and $\sin(n\varphi)$ or by their complex counterparts $\exp(\pm in\varphi)$. We use the real representation, since in particular in the case of a broken cylindrical symmetry of the QD, it provides more specific selection rules. The index n describes the order of the cylindrical multipole expansion, which is basically the number of nodal lines crossing the beam center (see Fig. 1). If we assume the QD to be on the beam axis, we can use the approximation $J_n(q_r r) \sim (q_r r)^n$ around the QD, since the beam profile is typically much larger than the QD, i.e., $q_r^{-1} \gg L_x/y$ (for details of this approximation see Appendix F). For linear polarizations along e_α (with $\alpha \in \{x, y, z\}$), an arbitrary beam profile close to the QD can be described in the basis

$$\tilde{\mathbf{A}}_{n, \theta, \alpha}(\mathbf{r}) = A_0 \left(\frac{r}{R_{\text{QD}}} \right)^n \cos(n\varphi - \theta) e_\alpha \quad (7)$$

with $R_{\text{QD}} = \frac{1}{4}(L_x + L_y)$. Here θ is introduced to describe the orientation reflected by the cosine or sine function for the

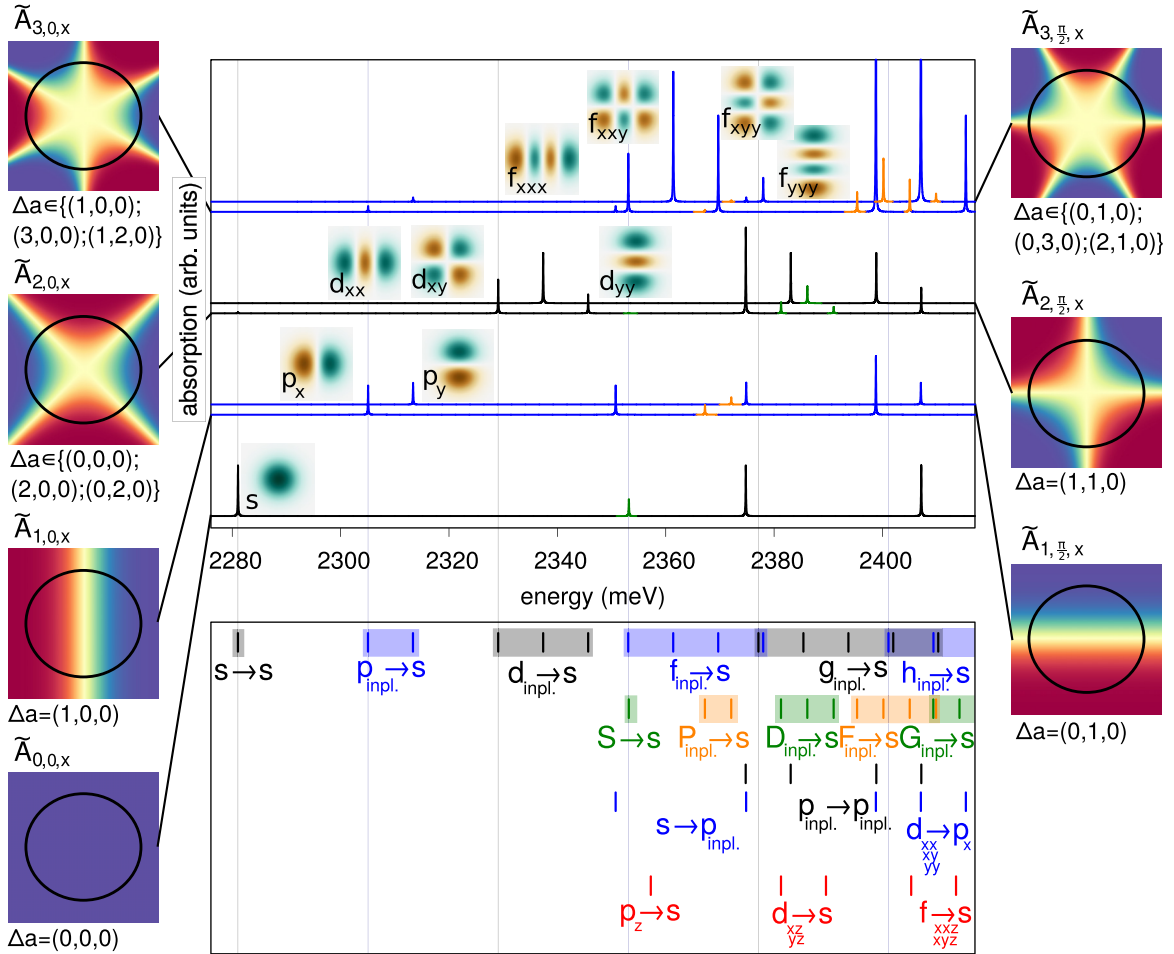


FIG. 2. The central box presents the absorption spectra for conventional homogeneous light fields (at the bottom) and the first few higher cylindrical multipole modes. Spectra are given for a QD in the simplified model ($\beta = 1$ and without Coulomb interaction and VBM, but with different confinement lengths $L_x > L_y$). In the box below, the energetic positions of all existing exciton states are marked by little bars at the corresponding transition energy. Different blocks of bars are vertically separated to improve visibility. Absorption lines are marked in the corresponding colors as a guide for the eye. At the sides we sketch the geometric profiles of the light field amplitudes around the QD in the $z = 0$ plane as well as the selection rules in the form $\Delta a = (\Delta a^x, \Delta a^y, \Delta a^z)$. Blue/red mark oppositional phases of the field. A linear polarization in the x direction is assumed (y -polarization equivalent). Between the spectra, we sketch the envelopes of the lowest few single-particle states in the $z = 0$ plane.

angular dependency and can take the value 0 or $\frac{\pi}{2}$. Typical geometries of those fields are plotted in Fig. 1 for e_x -polarized light.

III. REDUCED QD MODEL

Before studying our full model, it is instructive to consider a simple envelope function approach. For this we still consider an elongated QD confinement, however with equal confinement lengths for electron and hole (i.e., $\beta = 1$) and with uncoupled electron-hole pairs (without Coulomb interactions and VBM). A similar model was studied in Ref. [51] for a cylindrically symmetric model. To understand the absorption within this model, we first introduce the electronic level structure, then we discuss the selection rules, and finally we guide the reader to several important features in the observed spectra.

A. Electronic level structure

In the reduced QD model, products of the single-particle basis states $\Phi_{a,b\mu_b}$ already represent eigenstates of the system with exciton energies given by the sum of electron and hole energy. The energetic structure of these states is given by labeled bars in the box below the spectra in Fig. 2. At low energies, we find mainly those excitons composed of an in-plane excited HH and an electron in the s -like conduction band state, e.g., $s \rightarrow s$, $p_{\text{inpl.}} \rightarrow s$, $d_{\text{inpl.}} \rightarrow s$, ... (see first row of bars). Thereby states excited in different in-plane directions, like $p_x \rightarrow s$ and $p_y \rightarrow s$, form clusters in energy, since the diameter of the QD in the x and y directions is similar (but not equal). Because in these excitons the electron is always in the s -like state, the geometry of the exciton's envelope is defined by the geometry of the hole state (which is sketched for the lowest few excitons between the spectra in Fig. 2). Besides these HH excitons, at higher energies a similar level structure

occurs for the LH excitons (second row of bars). In addition, the electron can also be excited, resulting for example in $s \rightarrow p_{\text{inpl}}$ or $p_{\text{inpl}} \rightarrow p_{\text{inpl}}$ excitons (third row of bars). Because the QD is not a purely two-dimensional structure but has a finite height, we also get excitons excited in the z direction (fourth row of bars). One should note that within this reduced model each level (bar) has a fourfold spin degeneracy.

B. Symmetry considerations and selection rules

In the upper box of Fig. 2, we show absorption spectra for different cylindrical multipole modes [see Eq. (7)] for $n = 0, 1, 2, 3$. The spectra are displayed for x polarization; they are identical for y polarization, while for z polarization they can be deduced by setting the HH transitions to zero and upscaling the LH transitions by a factor of 4 (see Table I). The geometric profiles of the light field amplitudes in the $z = 0$ plane are sketched on the left (right) hand side of the spectra for $\theta = 0$ ($\theta = \frac{\pi}{2}$). The spectrum at the bottom ($n = 0$) represents the absorption of conventional light. There we see the $s \rightarrow s$, $S \rightarrow s$, $p_x \rightarrow p_x$, and $p_y \rightarrow p_y$ transitions. The restriction to these few states is caused by the simplifications in the reduced model, in particular the symmetric definition of electron and hole envelope wave functions via $\beta = 1$.

To understand the absorption patterns, we need to consider the transition matrix elements $M_{a_1, a_2; b_1, b_2}(\vec{A})$ [see Eq. (6)]. These are basically given by the overlap between the amplitude of the light field (given on the side of the spectra) and the envelope of the exciton. These overlaps and thereby the selection rules are easily estimated for several lower excitons by a visual comparison: As discussed above, the geometry of excitons containing an s -shell electron are mainly described by the geometry of the hole envelope, which is sketched for the corresponding exciton states between the spectra. Only if the parities of light field amplitude and envelope are equal in each direction may an absorption occur. As an example, the light field $\vec{A}_{1,0,x}$ is odd in the x and even in the y direction. This light field will just interact with excitons with the same parity, like the $p_x \rightarrow s$ exciton. The exciton $p_y \rightarrow s$, which is even in the x and odd in the y direction, has no overlap with $\vec{A}_{1,0,x}$ and accordingly no absorption line is visible. It turns out that the difference between the envelope quantum number of the exciton's hole and electron, namely $\Delta a^\alpha = |a_{\text{hole}}^\alpha - a_{\text{elec}}^\alpha|$, is a well-suited quantity to describe selection rules. With our graphical approach, we can easily deduce the selection rule that for an interaction with the field $\vec{A}_{1,0,x}$, the exciton has to fulfill Δa^x odd and Δa^y even. In fact, the selection rule can be further restricted to the explicit values $\Delta \mathbf{a} = (\Delta a^x, \Delta a^y, \Delta a^z) = (1, 0, 0)$. Accordingly just absorption lines for $p_x \rightarrow s$, $s \rightarrow p_x$, $P_x \rightarrow s$, and $d_{xx} \rightarrow p_x$ are observed in the given energetic range. The corresponding envelope selection rules are given below the field profiles.

An analytical derivation of the envelope selection rules for arbitrary cylindrical multipole modes is given in Appendix B. Summarized, we get a light-matter interaction if the following hold:

(1) For $\theta = 0$: The parity of Δa^x has to be the same as the parity of n , while Δa^y has to be even.

For $\theta = \frac{\pi}{2}$: The parity of Δa^x has to be different from the parity of n , while Δa^y has to be odd.

(2) $\sum_{v \in \{x,y\}} \Delta a^v \leq n$; $\Delta a^z = 0$.

(3) $\sum_{v \in \{x,y\}} (a_{\text{elec}}^v + a_{\text{hole}}^v) \geq n$. This third rule holds exactly only for $L_x = L_y$. However, one could stretch the light field to match the same oval form as the QD to restore this selection rule.

The first two “strong” envelope selection rules are considered for the rules given in Fig. 2.

C. Characteristic features of the absorption spectra

After this general introduction to the selection rules, we highlight some characteristic features of the absorption spectra in Fig. 2.

Selectivity. While the $p_x \rightarrow s/p_y \rightarrow s$ transitions can be accessed separately by different light modes, for higher $\text{HH}_{\text{inpl}} \rightarrow s$ envelope clusters no full selectivity between the different states is achieved. Here the parity determines which of the states are addressed by the same light field: For even n , all envelope states following the symmetry $\Delta \mathbf{a} = (\text{odd}, \text{odd}, \text{even}) = (\text{o}, \text{o}, \text{e})$ or $\Delta \mathbf{a} = (\text{e}, \text{e}, \text{e})$ are addressed together, and for odd n the states of the form $(\text{o}, \text{e}, \text{e})$ or $(\text{e}, \text{o}, \text{e})$. The parity of some selected states is given in Table II. This “reduced” selectivity is a side effect of the fact that the radial variation of the light field is effectively restricted to a power-law dependence over the size of the QD (see Appendix B, subsection on Hermite-Gaussian beam profiles).

Addressability. In a cylindrically symmetric QD, the $\text{HH}_{\text{inpl}} \rightarrow s$ transitions would give the energetically lowest possible transitions, caused by the third selection rule. This rule is slightly broken in the case of a broken cylindrical symmetry, causing for $n = 2$ the small $s \rightarrow s$ and $S \rightarrow s$ peaks and for $n = 3$ the small $p_{\text{inpl}} \rightarrow s$, $s \rightarrow p_{\text{inpl}}$, and $P_{\text{inpl}} \rightarrow s$ peaks (in Fig. 2 hardly visible without zooming into the figure).

In addition to the $\text{HH}_{\text{inpl}} \rightarrow s$ transitions, there are the corresponding $\text{LH}_{\text{inpl}} \rightarrow s$ transitions visible at higher energies. Furthermore, we find in the spectra the following:

(i) For $n = 0$ the $p_x \rightarrow p_x$ and $p_y \rightarrow p_y$ transitions.

(ii) For $n = 1$ the $s \rightarrow p_x/s \rightarrow p_y$ and $d_{xx} \rightarrow p_x/d_{xy} \rightarrow p_x$ transitions.

(iii) For $n = 2$ in addition to the already with $n = 0$ accessible $p_x \rightarrow p_x/p_y \rightarrow p_y$ also the $p_y \rightarrow p_x/p_x \rightarrow p_y$ transitions.

(iv) For $n = 3$ in addition to the already with $n = 1$ accessible $d_{xx} \rightarrow p_x/d_{xy} \rightarrow p_x$ also the $d_{yy} \rightarrow p_x$ transition.

Not reachable at this level of approximation are excitons with hole and electron in different excitation levels in the z direction ($\Delta a^z \neq 0$, marked in red). To enable such transitions, the light field needs to have a nodal plane perpendicular to the z direction which can be created, e.g., by a standing wave or an incidence of the beam from the side. Furthermore, at this level of approximation, each exciton level still has a fourfold spin degeneracy. Therefore, spin selection rules, even if they exist, do not show up in the spectra. Spin selection rules will become apparent in the next section.

The intensities of transitions excited in different directions (e.g., $p_x \rightarrow s$ and $p_y \rightarrow s$) are not equal. Because the interaction of higher modes with the QD results from the finite light field in the outer regions of the QD, and the state excited in the direction of the wider QD confinement (here $p_x \rightarrow s$) has larger contributions in these outer regions, the light-matter coupling is stronger for these states.

TABLE II. Parity (P^x, P^y, P^z) of the envelope part of exemplary electron-hole pair states for reflections at a plane with normal in the x , y , and z directions, respectively; o and e refer to odd and even parity, respectively.

Pair state	$s \rightarrow s$	$p_x \rightarrow s$	$p_y \rightarrow s$	$d_{xx} \rightarrow s$	$d_{xy} \rightarrow s$	$D_{xy} \rightarrow s$	$d_{yy} \rightarrow s$	$p_z \rightarrow s$	$s \rightarrow p_x$	$p_x \rightarrow p_x$	$p_x \rightarrow p_y$
(P^x, P^y, P^z)	(e,e,e)	(o,e,e)	(e,o,e)	(e,e,e)	(o,o,e)	(o,o,e)	(e,e,e)	(e,e,o)	(o,e,e)	(e,e,e)	(o,o,e)

When we rotate the orientation of the nodal planes for a fixed value of n , we get a continuous change between the two plotted spectra. This implies that one can determine the direction of elongation of the QD by an alignment of the light field to the case where the spectra are most selective.

IV. FULL QD MODEL

To get a more realistic idea of the absorption spectra, we now consider the full QD model by including Coulomb interactions and VBM. Furthermore we set $\beta = 1.15$ leading to hole basis states which are slightly more extended than the electron basis states. The resulting spectra are displayed in Fig. 3.

A. Electronic level structure

The level structure obtained from the full QD model is again shown by bars in the lower part of Fig. 3. In addition to a strong redshift (reflecting the exciton binding energy, mainly caused by CDI), the previously fourfold spin degeneracy is completely lifted. HH excitons like $s \rightarrow s$ are typically

separated into two energetically close so-called dark excitons (mainly consisting of ϵ_z and ϵ_0) and two energetically close bright excitons (mainly consisting of ϵ_x and ϵ_y) at higher energy. LH excitons like $S \rightarrow s$ are typically separated into one single exciton (mainly consisting of ϵ_0), two energetically close excitons (mainly consisting of $\epsilon_{\bar{x}}$ and $\epsilon_{\bar{y}}$), and a second single exciton at higher energy (mainly consisting of ϵ_z).

In addition, the envelopes of the eigenstates lose their simple geometrical character. In other words, the considered interactions (CDI, SRE, and VBM) mix the different basis states so that an exciton eigenstate is never a pure, e.g., $(s \rightarrow s)\epsilon_x$ state, but rather a mixture between, for example, $(s \rightarrow s)\epsilon_x$, $(d \rightarrow s)\epsilon_x$, $(S \rightarrow s)\epsilon_{\bar{x}}$, ... basis states. Typically, one of the basis state contributions dominates and can be used to describe the main character of the eigenstate. Here and in the following we take this dominant contribution to label and refer to the eigenstates.

B. Symmetry considerations and selection rules

Absorption spectra are plotted in the main part of Fig. 3 for different orders of the beams up to $n = 3$, different

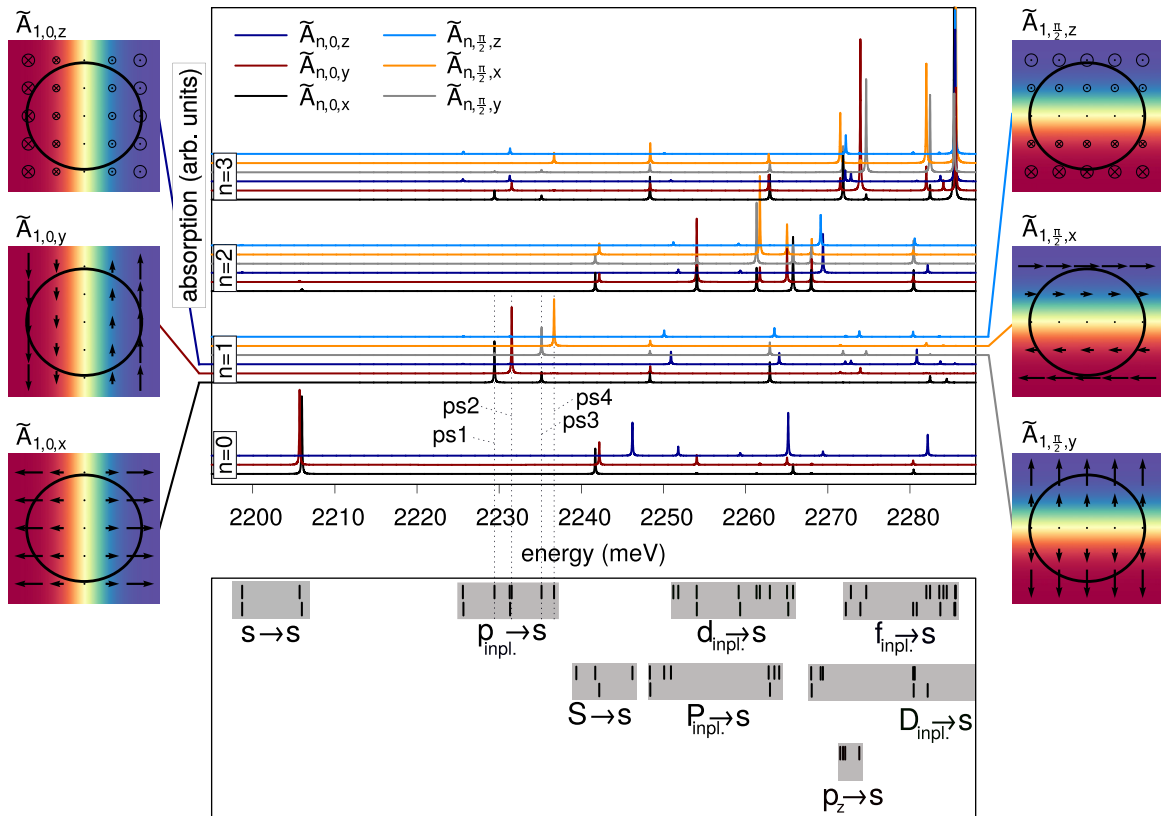


FIG. 3. Absorption spectra for a QD in the full model for different linear polarizations α and different orientations θ . In the box below, all existing exciton eigenstates are displayed in blocks labeled by the most appropriate envelope basis state.

orientations θ , and different polarizations e_α . In contrast to the reduced model (Fig. 2), the absorption spectra for x , y , and z polarization are now completely different; thus they are plotted separately. The light fields are drawn exemplarily on the left side of the spectra for the modes $\tilde{A}_{1,0,x/y/z}$ and on the right side for the modes $\tilde{A}_{1,\frac{\pi}{2},y/x/z}$.

The spectra are typically dominated by the peaks already observed in the reduced model. Especially the $\text{HH}_{\text{impl}} \rightarrow s$ transitions can still be well identified. Some additional small lines appear due to the coupling of different basis states (and also because here $\beta \neq 1$ has been taken). Although their oscillator strengths are typically small, in fact, within the full model *all* previously optically inaccessible eigenstates, such as envelope states with $\Delta a^z \neq 0$ or the dark HH and LH spin states, become optically accessible for excitation with an appropriate light field. To understand the characteristic features of the spectra, a better understanding of the state mixtures is necessary. Which states get mixed is best answered by symmetry considerations. The following discussion is based on the assumption of a threefold reflection symmetry. A discussion of the effects of a broken reflection symmetry can be found in Appendix D.

With the reflections \hat{R}_α at a plane through the QD center with a normal in direction $\alpha \in \{x, y, z\}$, we can define the parity P^α in the respective direction by

$$\hat{R}_\alpha |\Psi\rangle = P^\alpha |\Psi\rangle.$$

Here we need to consider the symmetry of the full states, i.e., envelope and Bloch state combined. The parity of the Bloch states is given in Table I, while the parity of the envelope states is given for exemplary states in Table II. Our model preserves a threefold reflection symmetry; accordingly, basis states with different P^x , P^y , or P^z are not coupled and our problem can be separated into eight subspaces. In the notation of group theory, our model has D_{2h} symmetry and the eigenstates are grouped according to the eight irreducible representations, as listed in Fig. 4.

Each of the eight subspaces contains basis states which can be excited by appropriate light fields; these are the enframed states in Fig. 4. Because in general all states in a subspace are mixed, all eigenstates become at least slightly optically active. However, selection rules with respect to the subspace still hold: a light mode $\tilde{A}_{n,\theta,\alpha}$ with given values of n , θ , and α just excites states within one subspace. In the following we will discuss the influence of the mixing for different classes of excitons. A detailed discussion of the question of which selection rules of the simplified model are broken by which interaction is given in Appendix C.

C. Characteristic features of the absorption spectra

Based on the listing of the possible state mixtures given in Fig. 4, we now discuss the characteristic features of the absorption spectra in Fig. 3 for different classes of excitons.

1. Excitons $\sim \epsilon_{x/\bar{x}}$ and $\sim \epsilon_{y/\bar{y}}$ with even Δa^z

Let us start the discussion with the class of excitons that comprises the standard, optically active excitons. Excitons $\sim \epsilon_{x/\bar{x}}$ and $\sim \epsilon_{y/\bar{y}}$ with even Δa^z (i.e., the encircled states in the

n even	$B_{2u}: (E,O,E)$		$A_u: (O,O,O)$	
	$(e,O,O) \epsilon_z$	$(e,O,O) \epsilon_{\bar{z}}$	$(O,O,e) \epsilon_z$	$(O,O,e) \epsilon_{\bar{z}}$
	$(O,e,O) \epsilon_0$	$(O,e,O) \epsilon_{\bar{0}}$	$(e,e,e) \epsilon_0$	$(e,e,e) \epsilon_{\bar{0}}$
	$(O,O,e) \epsilon_x$	$(O,O,e) \epsilon_{\bar{x}}$	$(e,O,O) \epsilon_x$	$(e,O,O) \epsilon_{\bar{x}}$
	$(e,e,e) \epsilon_y$	$(e,e,e) \epsilon_{\bar{y}}$	$(O,e,O) \epsilon_y$	$(O,e,O) \epsilon_{\bar{y}}$
n odd	$B_{3u}: (O,E,E)$		$B_{1u}: (E,E,O)$	
	$(O,e,O) \epsilon_z$	$(O,e,O) \epsilon_{\bar{z}}$	$(e,e,e) \epsilon_z$	$(e,e,e) \epsilon_{\bar{z}}$
	$(e,O,O) \epsilon_0$	$(e,O,O) \epsilon_{\bar{0}}$	$(O,O,e) \epsilon_0$	$(O,O,e) \epsilon_{\bar{0}}$
	$(e,e,e) \epsilon_x$	$(e,e,e) \epsilon_{\bar{x}}$	$(O,e,O) \epsilon_x$	$(O,e,O) \epsilon_{\bar{x}}$
	$(O,O,e) \epsilon_y$	$(O,O,e) \epsilon_{\bar{y}}$	$(e,O,O) \epsilon_y$	$(e,O,O) \epsilon_{\bar{y}}$
n odd	$A_g: (E,E,E)$		$B_{2g}: (O,E,O)$	
	$(e,e,e) \epsilon_z$	$(e,e,e) \epsilon_{\bar{z}}$	$(O,e,e) \epsilon_z$	$(O,e,e) \epsilon_{\bar{z}}$
	$(O,O,O) \epsilon_0$	$(O,O,O) \epsilon_{\bar{0}}$	$(e,O,e) \epsilon_0$	$(e,O,e) \epsilon_{\bar{0}}$
	$(O,e,e) \epsilon_x$	$(O,e,e) \epsilon_{\bar{x}}$	$(e,e,O) \epsilon_x$	$(e,e,O) \epsilon_{\bar{x}}$
	$(e,O,e) \epsilon_y$	$(e,O,e) \epsilon_{\bar{y}}$	$(O,O,O) \epsilon_y$	$(O,O,O) \epsilon_{\bar{y}}$
n odd	$B_{1g}: (O,O,E)$		$B_{3g}: (E,O,O)$	
	$(O,O,O) \epsilon_z$	$(O,O,O) \epsilon_{\bar{z}}$	$(e,O,e) \epsilon_z$	$(e,O,e) \epsilon_{\bar{z}}$
	$(e,e,O) \epsilon_0$	$(e,e,O) \epsilon_{\bar{0}}$	$(O,e,e) \epsilon_0$	$(O,e,e) \epsilon_{\bar{0}}$
	$(e,O,e) \epsilon_x$	$(e,O,e) \epsilon_{\bar{x}}$	$(O,O,O) \epsilon_x$	$(O,O,O) \epsilon_{\bar{x}}$
	$(O,e,e) \epsilon_y$	$(O,e,e) \epsilon_{\bar{y}}$	$(e,e,O) \epsilon_y$	$(e,e,O) \epsilon_{\bar{y}}$

Accessible by: $\tilde{A}_{n,0,x}/\tilde{A}_{n,\frac{\pi}{2},x}/\tilde{A}_{n,0,y}/\tilde{A}_{n,\frac{\pi}{2},y}/\tilde{A}_{n,0,z}/\tilde{A}_{n,\frac{\pi}{2},z}$

FIG. 4. Eight subspaces of exciton eigenstates defined by the three reflection symmetries in the x , y , and z directions (corresponding to the eight irreducible representations of the D_{2h} -symmetry group). For each subspace, the parity in the x , y , and z directions is given in capital letters (or the corresponding Mulliken symbol), followed by the eight corresponding combinations of the parities of envelope basis states (parities labeled in small letters) and parities of spin basis states (labeled by $\epsilon_z, \epsilon_{\bar{z}}, \dots$). Optically accessible basis states are encircled with the color referring to the coupling to specific light modes as given at the bottom of the Figure. The required parity of n is given for the upper and lower parts of the table. States accessible by plane-wave-like light are encircled by broader lines.

subspaces $B_{2u}, B_{3u}, A_g, B_{1g}$ in Fig. 4) are directly accessible by appropriate light fields and have been bright already in the reduced model. In fact, for $\Delta a^x = \Delta a^y = \Delta a^z = 0$ these are the standard HH and LH excitons which can be excited by plane waves. In our full model, the states are coupled to each other and, thus, they are not anymore exclusively addressable by the directly attributed light field, but (for $n \geq 1$) at least weakly also by a perpendicularly polarized and by a $\frac{\pi}{2}$ rotated light field. This is displayed in Fig. 4, where all subspaces, and all corresponding eigenstates, on the left are addressable by $\tilde{A}_{n,0,x}$ and $\tilde{A}_{n,\frac{\pi}{2},y}$ or by $\tilde{A}_{n,\frac{\pi}{2},x}$ and $\tilde{A}_{n,0,y}$.

As an example, it is instructive to consider the four ($p_{\text{impl}} \rightarrow s$) $\epsilon_{x/y}$ transitions. They can be identified in Fig. 3 as those four states with the strongest absorption peaks in the spectra for $\tilde{A}_{1,0,x}$, $\tilde{A}_{1,0,y}$, $\tilde{A}_{1,\frac{\pi}{2},y}$, and $\tilde{A}_{1,\frac{\pi}{2},x}$. They are coupled regarding $(p_x \rightarrow s)\epsilon_x \leftrightarrow (p_y \rightarrow s)\epsilon_y$ and $(p_x \rightarrow s)\epsilon_y \leftrightarrow (p_y \rightarrow s)\epsilon_x$ by an interplay between SRE and VBM. This

leads to approximate eigenstates (from low to higher energy)

$$\begin{aligned}
|\text{ps1}\rangle &= C_1|(p_x \rightarrow s)\epsilon_x\rangle + \tilde{C}_1|(p_y \rightarrow s)\epsilon_y\rangle, \\
|\text{ps2}\rangle &= C_2|(p_x \rightarrow s)\epsilon_y\rangle - \tilde{C}_2|(p_y \rightarrow s)\epsilon_x\rangle, \\
|\text{ps3}\rangle &= C_3|(p_y \rightarrow s)\epsilon_y\rangle - \tilde{C}_3|(p_x \rightarrow s)\epsilon_x\rangle, \\
|\text{ps4}\rangle &= C_4|(p_y \rightarrow s)\epsilon_x\rangle + \tilde{C}_4|(p_x \rightarrow s)\epsilon_y\rangle,
\end{aligned} \tag{8}$$

with real and positive coefficients C_j and \tilde{C}_j . For a strongly elongated QD we get $C_i \gg \tilde{C}_i$, while for $L_x = L_y$ we get $C_i = \tilde{C}_i$. In our case (VBM through Luttinger Hamiltonian without strain), the coupling $(p_x \rightarrow s)\epsilon_y \leftrightarrow (p_y \rightarrow s)\epsilon_x$ is weaker than $(p_x \rightarrow s)\epsilon_x \leftrightarrow (p_y \rightarrow s)\epsilon_y$ and the higher optical activity of $p_x \rightarrow s$ compared to $p_y \rightarrow s$ leads to the situation that just the admixture of $(p_x \rightarrow s)\epsilon_x$ to $(p_y \rightarrow s)\epsilon_y$ in state $|\text{ps3}\rangle$ is strongly noticeable by an additional peak in the $\tilde{A}_{1,0,x}$ spectrum. Other $(\text{HH}_{\text{impl}} \rightarrow s)\epsilon_{x/y}$ couple in a similar way (for $d_{\text{impl}} \rightarrow s$ see Appendix E).

2. Excitons $\sim \epsilon_z$ with even Δa^z

This class comprises the LH excitons with total spin zero which already in the simplified model can be excited by a field component $\sim e_z$. With mixing, these excitons (subspaces $A_u, B_{1u}, B_{2g}, B_{3g}$) couple via VBM to other states within the same subspace. However, all the other states in the respective subspace are dark. Therefore, they remain to be excitable selectively by the light fields $\tilde{A}_{n,\frac{\pi}{2},z}$ and $\tilde{A}_{n,0,z}$.

3. Excitons $\sim \epsilon_{z/0/\bar{0}}$ with even Δa^z

Without mixing, all excitons $\sim \epsilon_{z/0/\bar{0}}$ are dark because of the vanishing dipole moments of the Bloch basis states (see Table I). With mixing, all these excitons with even envelope parity in the z direction (subspaces $A_u, B_{1u}, B_{2g}, B_{3g}$) become slightly optically accessible by a coupling via VBM to the bright LH excitons $\sim \epsilon_{\bar{z}}$, which can be addressed by a light field with a longitudinal component. For each envelope, the spin states $\sim \epsilon_{0/\bar{0}}$ and $\sim \epsilon_{z/\bar{z}}$ are separately accessible by the light fields $\tilde{A}_{n,\frac{\pi}{2},z}$ and $\tilde{A}_{n,0,z}$. The concrete assignment can be deduced from Fig. 4.

As an example, let us consider here the accessibility of the initially dark $(d_{ij} \rightarrow s)\epsilon_{z/0}$ excitons. The $(d_{xx} \rightarrow s)\epsilon_z$ and $(d_{yy} \rightarrow s)\epsilon_z$ belonging to B_{1u} become bright via coupling to other states within B_{1u} , for instance to the bright states $(S \rightarrow s)\epsilon_{\bar{z}}$, $(D_{xx} \rightarrow s)\epsilon_{\bar{z}}$, and $(D_{yy} \rightarrow s)\epsilon_{\bar{z}}$. They are visible in both spectra $\tilde{A}_{0,0,z}$ and $\tilde{A}_{2,0,z}$. We note that the oscillator strengths depend on the individual state and QD geometry [48]; thus some excitons are not visible on a linear scale as used in Fig. 3.

In particular, the $(d_{yy} \rightarrow s)\epsilon_z$ exciton exhibits an exceptionally strong mixture with the bright $(S \rightarrow s)\epsilon_{\bar{z}}$ exciton. Accordingly, these two eigenstates dominate the spectrum for $n = 0$ and e_z polarization (see blue spectrum for $n = 0$ in Fig. 3). This coupling can be utilized for example for an efficient excitation scheme of the dark exciton ground state [61].

The $(d_{xx} \rightarrow s)\epsilon_0$ and $(d_{yy} \rightarrow s)\epsilon_0$ excitons, which have the symmetry $(e, e, e)\epsilon_0$ and are thereby belonging to A_u , are coupled to other states within A_u , for instance to the bright

states with symmetry $(o, o, e)\epsilon_{\bar{z}}$, like $(D_{xy} \rightarrow s)\epsilon_{\bar{z}}$. Accordingly, they are visible in the spectrum for $\tilde{A}_{2,\frac{\pi}{2},z}$.

The $(d_{xy} \rightarrow s)\epsilon_0$ excitons have the symmetry $(o, o, e)\epsilon_0$ and are thereby belonging to B_{1u} . They are coupled to other states within B_{1u} , for instance to the bright states with symmetry $(e, e, e)\epsilon_{\bar{z}}$, like $(S \rightarrow s)\epsilon_{\bar{z}}$, $(D_{xx} \rightarrow s)\epsilon_{\bar{z}}$, and $(D_{yy} \rightarrow s)\epsilon_{\bar{z}}$. They are visible in both spectra $\tilde{A}_{0,0,z}$ and $\tilde{A}_{2,0,z}$. Similarly, the $(d_{xy} \rightarrow s)\epsilon_z$ with the symmetry $(o, o, e)\epsilon_z$ (belonging to A_u) couple to the bright states with symmetry $(o, o, e)\epsilon_{\bar{z}}$, like $(D_{xy} \rightarrow s)\epsilon_{\bar{z}}$. Accordingly, they are visible in the spectrum for $\tilde{A}_{2,\frac{\pi}{2},z}$.

Although the different spin states of one envelope are selectively addressable, different envelopes within one group are in general not separately accessible; e.g., $(d_{xx} \rightarrow s)\epsilon_z$, $(d_{xy} \rightarrow s)\epsilon_0$, and $(d_{yy} \rightarrow s)\epsilon_z$ are all addressable by $\tilde{A}_{2,0,z}$.

4. Excitons $\sim \epsilon_{x/\bar{x}}$ and $\sim \epsilon_{y/\bar{y}}$ with odd Δa^z

As already mentioned, without mixing, excitons with odd Δa^z can only be excited by a light field which has a nodal plane perpendicular to the z direction. Therefore, they are dark for all the modes $\tilde{A}_{n,\theta,\alpha}$ propagating in the z direction, as considered here. Including mixing, these excitons [in the considered energetic range just the $(p_z \rightarrow s)\epsilon_{x/y}$ excitons] belong to the subspaces $A_u, B_{1u}, B_{2g}, B_{3g}$. They get separately accessible via couplings to bright LH excitons $\sim \epsilon_{\bar{z}}$ by the light fields $\tilde{A}_{n,0,z}$ and $\tilde{A}_{n,\frac{\pi}{2},z}$, polarized in growth direction. Again, the concrete assignment can be deduced from the above symmetry considerations, as given in Fig. 4.

In particular, in the case of $n = 1$ the $(p_z \rightarrow s)\epsilon_x$ and $(p_z \rightarrow s)\epsilon_y$ excitons get bright by couplings to $(P_x \rightarrow s)\epsilon_{\bar{z}}$ and $(P_y \rightarrow s)\epsilon_{\bar{z}}$, respectively, which is visible in the bunch of small peaks for $\tilde{A}_{1,0/\frac{\pi}{2},z}$.

5. Excitons $\sim \epsilon_{z/\bar{z}}$ and $\sim \epsilon_{0/\bar{0}}$ with odd Δa^z

Also these excitons are dark for all modes $\tilde{A}_{n,\theta,\alpha}$ considered here because of the their odd value of Δa^z . These excitons [in the considered energetic range just the $(p_z \rightarrow s)\epsilon_{z/0}$] belong to the subspaces $B_{2u}, B_{3u}, A_g, B_{1g}$. They couple via VBM to bright LH excitons $\sim \epsilon_{\bar{x}/\bar{y}}$ and become optically accessible by in-plane polarized light. For $n = 1$ this is visible in the bunch of small peaks at the corresponding energies in the spectra of $\tilde{A}_{1,0/\frac{\pi}{2},x/y}$. For a selective excitation see Sec. V.

V. QUANTITATIVE MEASUREMENT OF THE EXCITONIC EIGENSTATES

As we have seen in the previous sections, it is possible to identify certain eigenstates, e.g., the $\text{HH}_{\text{impl}} \rightarrow s$ transitions, from the absorption spectra of different cylindrical multipole modes. In fact, this identification of the spatial character of an eigenstate can be expanded to a quantitative measurement of the wave functions of all eigenstates. Here we emphasize that such a measurement will go beyond electron density measurements by accessing the wave function itself, thus also the spatial phase information of the state. It is clear that the required experimental conditions are rather challenging. However, before we discuss challenges in the experimental realization (see Sec. VI), we focus in this section on the basic theoretical idea behind the measurement.

The basic idea is to find a light field $\vec{A}(\mathbf{r}) = \sum_{m=1}^M a_m \vec{A}_m(\mathbf{r})$ with $\sum_{m=1}^M |a_m|^2 = 1$ which maximizes the absorption intensity of a considered eigenstate approximately described by $|\Psi\rangle \approx \sum_{n=1}^N c_n |n\rangle$ with $\sum_{n=1}^N |c_n|^2 = 1$ and $|n\rangle$ being a suitable set of orthogonal basis states. The absorption intensity [see Eq. (6)]

$$I \sim |\langle \Psi | \hat{H}_Y(\vec{A}) | 0 \rangle|^2 = \left| \sum_{m=1}^M \sum_{n=1}^N a_m \underbrace{\langle n | \hat{H}_Y(\vec{A}_m) | 0 \rangle}_{\alpha_{m,n}} c_n^* \right|^2 \quad (9)$$

can be maximized with respect to the constraint $\sum_{m=1}^M |a_m|^2 = 1$ with the result [62]

$$a_m = \frac{\sum_{n=1}^N \alpha_{m,n}^* c_n}{\sqrt{\sum_{m=1}^M \left| \sum_{n=1}^N \alpha_{m,n}^* c_n \right|^2}} \quad (10)$$

with $\alpha_{m,n}$ defined in Eq. (9). Thus, without normalization, the coefficients of the light field a_m with maximal absorption into a state defined by the coefficients c_n can be derived by a simple matrix multiplication $a_m = \sum_{n=1}^N \alpha_{m,n}^* c_n$.

It should be noted that in the absence of an external magnetic field, as studied here, all eigenstates can be taken to be real. Furthermore, the basic light modes [Eq. (7)] are real, hence $\alpha_{m,n}$ and c_n are real. Therefore it is sufficient to restrict ourselves to real coefficients a_m .

To measure an eigenfunction, we propose to vary the light field (i.e., a_m) until a maximum in the absorption is found. From these a_m one can derive the eigenstate, i.e., the coefficients c_n , if Eq. (10) can be inverted. Therefore we need to include at least $M = N$ multipole modes in the measurement. A similar measurement is known for polarization-sensitive absorption measurements, where the complex coefficients c_x and c_y of a spin state $c_x \epsilon_x + c_y \epsilon_y$ can be deduced from the different orientations of linear polarization and the degree between linear and circular polarization. In this sense, we present a generalized polarization measurement, which accesses in addition to the spin degree of freedom also the spatial degree of freedom.

A. Exemplary demonstration of the measurement for the $(p_{\text{impl}} \rightarrow s)\epsilon_{x/y}$ excitons

The measurement is here demonstrated with the $(p_{\text{impl}} \rightarrow s)\epsilon_{x/y}$ excitons, while a second example is provided for $d_{\text{impl}} \rightarrow s$ excitons in Appendix E. To start with, we consider state |ps3⟩ [see Eq. (8)], which is mainly excitable by the light fields $\vec{A}_{1,0,x}$ and $\vec{A}_{1,\frac{\pi}{2},y}$ (see Fig. 3). Within our scheme, one would measure the absorption intensity for all possible real-valued superpositions $a_1 \vec{A}_{1,0,x} + a_2 \vec{A}_{1,\frac{\pi}{2},y}$ of these two fields. These superpositions include, for example, radially polarized fields and can be thought of as continuous transitions between the fields plotted in the insets of Fig. 5(a). In Fig. 5, the absorption intensity of state |ps3⟩ is plotted in a polar plot with $\tan(\xi) = \frac{a_2}{a_1}$. As a result, the light field

$$0.52 \vec{A}_{1,0,x} - 0.85 \vec{A}_{1,\frac{\pi}{2},y}$$

causes the strongest absorption of state |ps3⟩.

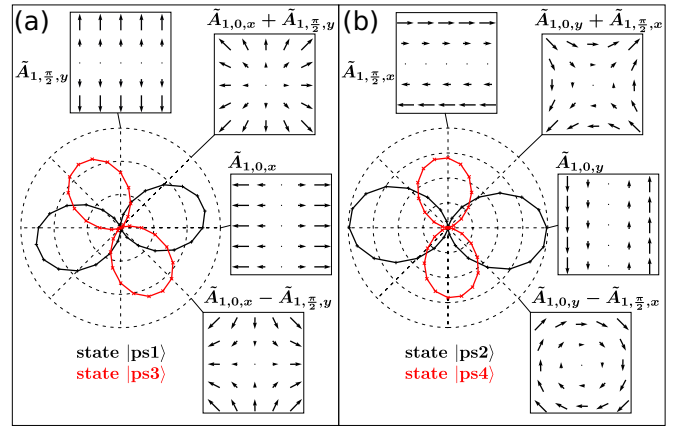


FIG. 5. Intensity of the $(p_{\text{impl}} \rightarrow s)\epsilon_{x/y}$ eigenstates for different superpositions of $\vec{A}_{1,0,x}$ and $\vec{A}_{1,\frac{\pi}{2},y}$ [$\vec{A}_{1,0,y}$ and $\vec{A}_{1,\frac{\pi}{2},x}$] in (a) [(b)]. The insets display the corresponding field profiles.

To obtain the related electronic state from this field, we need to assume an electronic basis $|n\rangle$. Since we just measured the absorption of two light modes, we need to restrict this basis to two states. Here we assume $|1\rangle = |(p_x \rightarrow s)\epsilon_x\rangle$ and $|2\rangle = |(p_y \rightarrow s)\epsilon_y\rangle$, which are strongly excitable by the considered light fields. We could also assume higher basis states like $s \rightarrow p$, $P \rightarrow s$, $d \rightarrow p$, etc., which also couple noticeably to the measured light fields (see Fig. 2). However, these basis states are at higher energies and not supposed to be strongly coupled to a state at the energy of |ps3⟩. If stronger contributions of these basis states are to be assumed within the considered eigenstate, additional higher light modes need to be considered.

The matrix elements $\alpha_{m,n}$ can be calculated from the basis. In our case, $\vec{A}_{1,0,x}$ just excites $(p_x \rightarrow s)\epsilon_x$ and $\vec{A}_{1,\frac{\pi}{2},y}$ just $(p_y \rightarrow s)\epsilon_y$ and we get [63] $\alpha_{1,1} = 1.0013$, $\alpha_{2,2} = 0.7441$, and $\alpha_{1,2} = \alpha_{2,1} = 0$. From Eq. (10) we calculate $\frac{c_2}{c_1} = \frac{\alpha_{1,1}}{\alpha_{2,2}} \frac{a_2}{a_1}$. With this, the state deduced from the “measurement” would read

$$|\text{ps3}\rangle_{\text{meas}} = 0.42|(p_x \rightarrow s)\epsilon_x\rangle - 0.91|(p_y \rightarrow s)\epsilon_y\rangle.$$

The “exact” state is

$$|\text{ps3}\rangle_{\text{exact}} = 0.874[0.38|(p_x \rightarrow s)\epsilon_x\rangle - 0.92|(p_y \rightarrow s)\epsilon_y\rangle] + 0.463|\text{rest-bright}\rangle + 0.149|\text{rest-dark}\rangle. \quad (11)$$

We find that the agreement between the “measured” and “exact” state is reasonably good. In particular, the relative phase between the two basis states, i.e., the minus sign, is correctly reproduced. Also the weights between the two states are well described by the measurement. The inaccuracy of the measurement is caused by contributions of higher basis states. $0.149^2 \approx 2\%$ are higher basis states which are optically not accessible (|rest-dark⟩). Thus their coefficients cannot be accessed in general. $0.463^2 \approx 21\%$ are higher basis states which are optically accessible (|rest-bright⟩). When considering higher light modes, most of their coefficients can be determined (however the coefficients of two basis states with interchanged particle states, like $p_x \rightarrow s$ and $s \rightarrow p_x$ for $\beta = 1$, cannot be distinguished). Because some contributions of |rest-bright⟩ are also addressable by the measured light modes,

the relative contribution of $(p_x \rightarrow s)\epsilon_x$ and $(p_y \rightarrow s)\epsilon_y$ is slightly incorrect. The inaccuracy in terms of the angle ξ between the “measured” eigenstate and the “exact” eigenstate in Eq. (11) without higher terms is less than 4° . This angle should not be misunderstood as a spatial direction, like in pure polarization measurements, but as a visualization of a superposition like on a Bloch sphere (in the complex case). This generalized Bloch sphere has $2M - 1$ dimensions.

Similar measurements can be done for the other $(p_{\text{impl}} \rightarrow s)\epsilon_{x/y}$ states, as shown in Fig. 5. The measured state $|\text{ps1}\rangle$ would read

$$|\text{ps1}\rangle_{\text{meas.}} = 0.96|(p_x \rightarrow s)\epsilon_x\rangle + 0.28|(p_y \rightarrow s)\epsilon_y\rangle,$$

while the exact state reads

$$|\text{ps1}\rangle_{\text{exact}} = 0.839[0.95|(p_x \rightarrow s)\epsilon_x\rangle + 0.32|(p_y \rightarrow s)\epsilon_y\rangle] + 0.527|\text{rest-bright}\rangle + 0.137|\text{rest-dark}\rangle. \quad (12)$$

Compared to state $|\text{ps3}\rangle$, here we get a smaller and in-phase mixture of the basis states $(p_x \rightarrow s)\epsilon_x$ and $(p_y \rightarrow s)\epsilon_y$.

The states $|\text{ps2}\rangle$ and $|\text{ps4}\rangle$ are nearly pure $(p_x \rightarrow s)\epsilon_y$ and $(p_y \rightarrow s)\epsilon_x$ basis states, respectively. From the measurement, one would get the states

$$|\text{ps2}\rangle_{\text{meas.}} = 1.00|(p_x \rightarrow s)\epsilon_y\rangle - 0.09|(p_y \rightarrow s)\epsilon_x\rangle,$$

$$|\text{ps4}\rangle_{\text{meas.}} = 0.07|(p_x \rightarrow s)\epsilon_y\rangle - 1.00|(p_y \rightarrow s)\epsilon_x\rangle,$$

while the “exact” states read

$$|\text{ps2}\rangle_{\text{exact}} = 0.886[1.00|(p_x \rightarrow s)\epsilon_y\rangle - 0.01|(p_y \rightarrow s)\epsilon_x\rangle] + 0.447|\text{rest-bright}\rangle + 0.125|\text{rest-dark}\rangle,$$

$$|\text{ps4}\rangle_{\text{exact}} = 0.886[0.01|(p_x \rightarrow s)\epsilon_y\rangle + 1.00|(p_y \rightarrow s)\epsilon_x\rangle] + 0.442|\text{rest-bright}\rangle + 0.139|\text{rest-dark}\rangle. \quad (13)$$

For all $p_{\text{impl}} \rightarrow s$ states we thus find that our proposal reconstructs the exciton wave function between the participating states within reasonable accuracy. We stress that our proposal can retrieve the relative phases between the different spatial contributions, i.e., the phase field or wave function of the exciton. Thereby, we go beyond measurements of electron densities.

B. Notes regarding the proposed measurement strategy

When using our proposal, one should keep the following things in mind:

(1) A global phase is (of course) not accessible.

(2) We are measuring the excitonic wave function, but we cannot determine whether the electron or the hole is in a certain state. In other words, we cannot distinguish between contributions of, e.g., $p_x \rightarrow s$ and $s \rightarrow p_x$ basis states for $\beta = 1$. To understand this statement, we should recapitulate that the envelope part of the light-matter interaction is defined by

$$M_{a_1, a_2; b_1, b_2}(\tilde{A}) = \int d^3R \Phi_{a_1, b_1}^*(\mathbf{R}) \Phi_{a_2, b_2}(\mathbf{R}) \tilde{A}(\mathbf{R})$$

[see Eq. (6)]. Thus, the light field does not “see” the electron-hole-pair envelope basis state

$$\Phi_{a_1, a_2; b_1, b_2}^{\text{exciton}}(\mathbf{r}_{\text{hole}}, \mathbf{r}_{\text{elec}}) = \Phi_{a_1, b_1}^{\text{hole}*}(\mathbf{r}_{\text{hole}}) \Phi_{a_2, b_2}^{\text{elec}}(\mathbf{r}_{\text{elec}}),$$

but “just” the wave function $\Phi_{a_1, a_2; b_1, b_2}^{\text{exciton}}(\mathbf{r}_{\text{hole}}, \mathbf{r}_{\text{elec}})$ with $\mathbf{r}_{\text{hole}} = \mathbf{r}_{\text{elec}}$. For $\beta = 1$ and real-valued envelope functions, we get $\Phi_{a_1, a_2; b_1, b_2}^{\text{exciton}}(\mathbf{r}, \mathbf{r}) = \Phi_{a_2, a_1; b_2, b_1}^{\text{exciton}}(\mathbf{r}, \mathbf{r})$. Thus, it is not determinable whether the electron is in state a_1 and the hole in state a_2 , or vice versa. The requirement $\beta = 1$ defines just a convenient basis, where it is obvious that $\alpha_{m,n}$ is never invertible for, e.g., $p_x \rightarrow s$ and $s \rightarrow p_x$ basis states and any set of light fields. $\beta \neq 1$ does not change this statement in general, but just introduces nonorthonormal basis states for electrons and holes which make it harder to see whether $\alpha_{m,n}$ can be inverted.

(3) The coefficients of dark basis states cannot be determined, also due to the required invertibility of $\alpha_{m,n}$.

(4) The measurement is not restricted by the diffraction limit.

There are several possible applications closely related to this measurement:

(1) One can tune the light field geometry to get a maximal absorption into a certain state.

(2) The measurement of the exciton wave function allows one to draw conclusions about the QD’s geometry.

(3) A standard polarization-sensitive absorption measurement allows the readout of the spin degree of freedom of an electronic state within a QD. Such a measurement is typically the basis to use the spin as a storage for quantum information. In the same sense, the proposed generalized polarization measurement could pave the way to use the infinite spatial degree of freedom to store quantum information within a QD. Here, the problem of quickly decaying higher exciton states requires further research. However, at least for $n = 1$ relatively long lived metastable trion triplet states [31] are available.

(4) The selectivity of an optical excitation can be increased by a suitable superposition of cylindrical multipole modes. This is equivalent to polarization-selective excitation when energetic selectivity is not possible, and might be similarly powerful.

It is instructive to consider this measurement from an alternative perspective: We obtain the absorption intensity (neglecting the spin)

$$\left| \int d^3R \Phi_{\text{exc}}(\mathbf{R}, \mathbf{R}) \tilde{A}(\mathbf{R}) \right|^2 \quad (14)$$

for arbitrary light fields $\tilde{A}(\mathbf{R})$. The maximal intensity is expected for $\tilde{A}(\mathbf{R}) = \Phi_{\text{exc}}^*(\mathbf{R}, \mathbf{R})$; thus, the full complex exciton wave function $\Phi_{\text{exc}}(\mathbf{R}, \mathbf{R})$ can be measured by tuning the form of the light field until the intensity is maximized.

VI. REALISTIC LIGHT FIELDS

A. Notes on the experimental feasibility

To estimate the experimental feasibility of our proposal, we discuss the intensity of the absorption for higher n . Throughout this paper, the amplitude of the light fields is $\sim (\frac{r}{R_{\text{QD}}})^n$ [Eq. (7)]. r leads to contributions to the light-matter coupling strength on the order of R_{QD} , resulting in a scaling of the intensity $\sim (\frac{R_{\text{QD}}}{R_{\text{QD}}})^{2n} = 1$, leading to the comparable intensities of the different orders. However, the natural scaling can be deduced, for instance, from Bessel beams and is proportional to $\frac{(q \cdot r)^n}{2^n n!}$ (see Appendix F). The expected intensity for

a light field of order n is thus $\sim (\frac{q_r R_{\text{QD}}}{2n})^n$, as in Eq. (15) of Ref. [51].

q_r is fixed via $\sqrt{q_r^2 + q_z^2} = \frac{n_r E}{\hbar c_0}$ with the excitation energy $E = 2.2$ eV, a factor describing the beamwidth $\frac{q_r}{q_z} = 1$ [64] and the refractive index of CdSe of $n_r \approx 2.8$ [65] to $q_r \approx \frac{1}{45 \text{ nm}}$. With an average QD radius of $R_{\text{QD}} = 2.7$ nm and fixed A_0 , the intensity of the peaks is reduced by a factor $\sim 10^{-3}$, $\sim 10^{-7}$, $\sim 10^{-11}$, ... with order $n = 1, 2, 3, \dots$ of the light mode. We should highlight that optimizations are possible in regard of $\frac{q_r}{q_z}$, the QD radius R_{QD} , the excitation energy E , the diffraction index n_r , or by turning up A_0 for higher n . Instead of far-field beams, also near fields created, e.g., by laser-illuminated metal tips [49] could be used.

The proposed measurements of the wave function in Sec. V require in general a combination of light field modes of different order. Since the oscillator strength of these light modes differs by several orders of magnitude, the proposed measurement requires in general a very accurate adjustment of the light mode intensities over several orders of magnitude. However, in the special case of the measurement presented in Sec. V, just light modes of the same order (here $n = 1$) are utilized; thus “just” a good suppression of the $n = 0$ modes is required.

We assume to illuminate a single QD. If other QDs are within the diameter of the beam, their absorption lines need to be energetically well separated from those of the studied QD to prevent parasitic effects. The alignment between QD center and the center of the beam profile is important [66]. If we shift the light field around R_{misfit} away from the QD center, we get the substitution $(\frac{r}{R_{\text{QD}}})^n \rightarrow (\frac{r - R_{\text{misfit}}}{R_{\text{QD}}})^n$, which causes for example the additional plane-wave-like absorption peaks with a relative intensity on the order of $(\frac{R_{\text{misfit}}}{R_{\text{QD}}})^n$. Therefore for pure light modes of order n with a misalignment of $R_{\text{misfit}} = R_{\text{QD}}$, we already expect similar absorption intensities of plane-wave-like absorption patterns and the intended patterns for the light field of order n .

B. Solenoidal fields

Up to now we considered just convenient components of light fields. Realistic light fields need to be solenoidal in free space, which is clearly not the case for modes like $\tilde{A}_{1,0,x}(\mathbf{r}, t) \sim x e_x$. A well-defined theoretical basis to describe light fields is given by Bessel beams, which constitute an exact and complete solution of the vectorial Helmholtz equation. Although Bessel beams have an infinite radial extension, there are several experimentally realized approximations [67–69]. Around the beam axis, Bessel beams can be described by a simple superposition of a few cylindrical multipole modes. In the following, we will discuss these superpositions for several different representations of Bessel beams, which are given explicitly in Appendix F.

First, we consider propagating beams, i.e., propagating light fields with a finite extension of their beam profile. For an exact representation, one always has to combine a component polarized perpendicular to the propagation direction, i.e., polarized in the x/y direction, and additionally a component polarized along the propagation direction, i.e., the z direction. In our case, we need to combine the modes $\tilde{A}_{n,\theta,x}$ with

$\frac{q_r}{q_z} \tilde{A}_{n\pm 1,\theta,z}$ as well as the modes $\tilde{A}_{n,0/\pi/2,y}$ with $\frac{q_r}{q_z} \tilde{A}_{n\pm 1,\pi/2/0,z}$ [see Eqs. (F4) in Appendix F]. While the modes $\tilde{A}_{n,\theta,x/y}$ are scaled on the order of $(q_r R_{\text{QD}})^n$, the leading mode with polarization in the z direction ($\frac{q_r}{q_z} \tilde{A}_{n-1,\theta,z}$) is on the order of $\frac{q_r}{q_z} (q_r R_{\text{QD}})^{n-1}$. Accordingly $\tilde{A}_{n,\theta,x/y}$ is about a factor $q_z R_{\text{QD}}$ smaller than $\frac{q_r}{q_z} \tilde{A}_{n\pm 1,\theta,z}$. Because q_z has an upper limit of $\frac{n_r E}{\hbar c_0}$ even for the undesired case $\frac{q_r}{q_z} = 0$, we get $q_z R_{\text{QD}} < 0.08$. Therefore always the term polarized in the z direction dominates at the beam axis (except for $n = 0$). For our standard case $\frac{q_r}{q_z} = 1$ we get $q_z R_{\text{QD}} \approx 0.06$. The absorption spectra of the combined realistic modes can be deduced by a combination of the spectra for $\tilde{A}_{n,\theta,x}$ and $\tilde{A}_{n\pm 1,\theta,z}$ ($\tilde{A}_{n,0/\pi/2,y}$ and $\tilde{A}_{n\pm 1,\pi/2/0,z}$). If a threefold reflection symmetry is present, we can simply add the spectra, while with broken reflection symmetry in the z direction, an eigenstate might be addressable by both, x/y - and z -polarized modes, where constructive/destructive interference needs to be considered. This combination of spectra reduces the possibility for selective excitation. States excitable by $\tilde{A}_{n,\theta,x}$ and $\tilde{A}_{n\pm 1,\theta,z}$ ($\tilde{A}_{n,0/\pi/2,y}$ and $\tilde{A}_{n\pm 1,\pi/2/0,z}$) cannot be accessed separately anymore; for example consider state $|\text{ps}1\rangle$ (addressable by $\tilde{A}_{1,0,x}$) and the $(S \rightarrow s)\epsilon_z$ -like eigenstate (addressable by $\tilde{A}_{0,0,z}$). Furthermore, the states addressable by the much stronger z -polarized fields will always dominate the spectra. The measurement of the wave functions via Eq. (10) is not affected if there is a reflection symmetry in the z direction. In that case, there is no coupling between eigenspaces excitable by light polarized in the x/y direction and the z direction (see Fig. 4). If the reflection symmetry in the z direction is broken, such couplings are possible. For example, a small admixture of $(S \rightarrow s)\epsilon_z$ (excitable by $\tilde{A}_{0,0,z}$) occurs within state $\text{ps}1$ (excitable by $\tilde{A}_{1,0,x}$ and $\tilde{A}_{1,\pi/2,y}$). As we saw, the mode $\tilde{A}_{1,0,x}$ is always superposed with a much stronger mode $\tilde{A}_{0,0,z}$; thus the small admixture of $(S \rightarrow s)\epsilon_z$ can have a significant impact on the absorption intensity, which would distort the measurement as presented in Sec. V. To restore a correct measurement of the wave function, one could include a third light field mode [e.g., the combined field of $\tilde{A}_{3,\pi/2,y}$ and $\tilde{A}_{2,0,z}$, which mainly excites $(S \rightarrow s)\epsilon_z$] into the measurement and explicitly consider the $(S \rightarrow s)\epsilon_z$ basis state in the evaluation of Eq. (10). We conclude that the measurement is not hindered in general, but requires more effort.

The omnipresent strong z -polarized component vanishes in certain cases within another representation of Bessel beams. To describe such a representation, we first define an alternative multipole expansion via

$$\begin{aligned} \tilde{A}_{n,\theta,xy}(\mathbf{r}, t) &= A_0 \left(\frac{r}{R_{\text{QD}}} \right)^n [\cos(n\varphi - \theta) \mathbf{e}_x - \sin(n\varphi - \theta) \mathbf{e}_y], \\ \tilde{A}_{n,\theta,\tilde{xy}}(\mathbf{r}, t) &= A_0 \left(\frac{r}{R_{\text{QD}}} \right)^n [\cos(n\varphi - \theta) \mathbf{e}_x + \sin(n\varphi - \theta) \mathbf{e}_y]. \end{aligned} \quad (15)$$

These modes still have to be combined with z -polarized modes to obtain realistic fields. We have to combine the modes $\tilde{A}_{n,\theta,xy}$ with $\tilde{A}_{n+1,\theta,z}$ as well as the modes $\tilde{A}_{n+1,\theta,y}$ with $\tilde{A}_{n,\theta,z}$ [see Eqs. (F2) in Appendix F]. Thus, in the first case the terms with x/y polarization $\tilde{A}_{n,\theta,xy}$ dominate and the z -polarized component is negligible, while in the second case the

z -polarized component still prevails (except for $n = 0, \theta = \frac{\pi}{2}$). The above-described problems with the undesired admixed modes are just banned for certain special cases.

To avoid the undesired mixture of different multipole modes, one can consider standing waves. In fact, standing waves are created standardly in various microcavities built around QDs to increase the light-matter coupling [70,71]. Higher Hermite-Gaussian and Laguerre-Gaussian modes were found in hemispherical microcavities [4]. For standing waves we can position the QD into a nodal line of the field in the z direction and get the fields [see Eq. (F5) in Appendix F]

$$\begin{aligned}\tilde{\mathbf{A}}_{n,\theta}^x(\mathbf{r}, t) &= A_0(t) \frac{r^n}{R_{\text{QD}}^n} \left\{ \cos(n\varphi - \theta) \mathbf{e}_x \right. \\ &\quad \left. - \frac{nz}{r} \cos[(n-1)\varphi - \theta] \mathbf{e}_z \right\}, \\ \tilde{\mathbf{A}}_{n,\theta}^y(\mathbf{r}, t) &= A_0(t) \frac{r^n}{R_{\text{QD}}^n} \left\{ \cos(n\varphi - \theta) \mathbf{e}_y \right. \\ &\quad \left. + \frac{nz}{r} \sin[(n-1)\varphi - \theta] \mathbf{e}_z \right\}, \\ \tilde{\mathbf{A}}_{n,\theta}^z(\mathbf{r}, t) &= A_0(t) \frac{r^n}{R_{\text{QD}}^n} \cos(n\varphi - \theta) \mathbf{e}_z.\end{aligned}\quad (16)$$

The additional terms $\sim z\mathbf{e}_z$ are of the same order as the x/y -polarized terms and induce transitions into LH excitons excited in the z direction, like $P_z \rightarrow s$, $D_{xz} \rightarrow s/D_{yz} \rightarrow s$, $F_{xxz} \rightarrow s/F_{yyz} \rightarrow s/F_{yyz} \rightarrow s$, etc. Those states are well above the considered energetic range and weakly coupled to the studied transitions. Thus, the absorption spectra of the previous sections hold in good agreement also for the realistic light fields of Eq. (16).

VII. CONCLUSION

We have analyzed the absorption of spatially structured light beams by a QD. We focused on cylindrical multipole transitions and derived analytical selection rules for a simplified QD model. We have studied the coupling mechanisms via Coulomb interactions and valence band mixing, which lead to the optical addressability of all electronic eigenstates of the QD. Within this extended model, we analyzed the possibility to tailor the optical activity of certain states by varying the spatial shape of the exciting light field. Thereby we explored a way to excite the QD's eigenstates selectively, without the need of spectral separation. This way is similar to spin-selective excitation and could help to overcome the limits in time resolution of pump-probe experiments required by the desired energy selectivity. Furthermore, we proposed a method to measure the excitonic wave function of arbitrary eigenstates, including relative spatial phases, thereby going beyond electron density measurements. Such a measurement is the prerequisite to use the infinite spatial degree of freedom for QD-based quantum information technology. We explored the measurement of the wave function of the first excited exciton states in detail and estimated the precision. The experimental feasibility of the proposed techniques as well as different possibilities to realize cylindrical multipole modes

are discussed by a comparison with different representations of Bessel beams.

ACKNOWLEDGMENTS

G.F.Q. thanks the ONRG for financial support through NICOP grant N62909-18-1-2090.

APPENDIX A: SIMILARITY BETWEEN THE MATRIX ELEMENTS OF \hat{p} AND \hat{r}

Using the identity $\hat{p}_\alpha = -i\frac{m_0}{\hbar}[\hat{r}_\alpha, \hat{H}_0]$ with $\hat{H}_0 = \frac{\hat{p}^2}{2m} + V(\hat{r})$ being the Hamiltonian within the bulk crystal as well as the assumption that $\langle \hat{r} | b \rangle = u_b(\mathbf{r})$ are eigenfunctions of \hat{H}_0 (at the Γ point) and E_b the corresponding eigenenergies, we deduce that

$$\begin{aligned}\mu_{b_1, b_2}^\alpha &= e \langle b_1 | \frac{\hat{p}_\alpha}{m_0} | b_2 \rangle = -ie \frac{1}{\hbar} \langle b_1 | [\hat{r}_\alpha, \hat{H}_0] | b_2 \rangle \\ &= -ie \frac{1}{\hbar} \langle b_1 | \hat{r}_\alpha \hat{H}_0 - \hat{H}_0 \hat{r}_\alpha | b_2 \rangle \\ &= -ie \frac{E_{b_2} - E_{b_1}}{\hbar} \langle b_1 | \hat{r}_\alpha | b_2 \rangle\end{aligned}$$

with $-e \langle b_1 | \hat{r}_\alpha | b_2 \rangle$ representing the dipole moments in the typical form.

APPENDIX B: ANALYTICAL SELECTION RULES AND LIMITS OF THE SELECTIVITY

The optical selection rules between envelopes described by Hermite-Gaussian functions $\Phi_{a,b}$ are requested. Therefore we need to solve the integral [see Eq. (6)]

$$\mathbf{M}_{a_1, a_2; b_1, b_2}(\tilde{\mathbf{A}}) = \int d^3R \Phi_{a_1, b_1}^*(\mathbf{R}) \tilde{\mathbf{A}}(\mathbf{R}) \Phi_{a_2, b_2}(\mathbf{R}).$$

Here we focus on the case $\beta = 1$, which allows us to neglect the band index b . For certain expansions of the light field $\tilde{\mathbf{A}}(\mathbf{R})$, compact analytical selection rules can be given.

Power functions. For an expansion into power functions $\tilde{\mathbf{A}}_{n_x, n_y, n_z}^{\text{Power}}(\mathbf{R}) = \tilde{A}_0 x^{n_x} y^{n_y} z^{n_z}$, the integral can be decomposed into three one-dimensional integrals, which can be solved by ladder operator algebra. With $\Delta a^\alpha = |a_{\text{hole}}^\alpha - a_{\text{elec}}^\alpha|$, the selection rules read as follows:

- (1) The parity of Δa^α and n_α has to be the same.
- (2) $\Delta a^\alpha \leq n_\alpha$.

It is possible to tailor selection rules within certain limits. As an example, it is possible to deactivate an arbitrary transition $a^\alpha \rightarrow \tilde{a}^\alpha$ by an adequate superposition of the power functions $\alpha^{|a-\tilde{a}|}$ and $\alpha^{|a-\tilde{a}|+2}$.

Hermite polynomials. The question arises as to whether it might be possible to increase the selectivity by an optimized set of light fields. To explore the theoretical limit of such a selectivity, it is instructive to expand the light fields into Hermite polynomials H_n via $\tilde{\mathbf{A}}_{n_x, n_y, n_z}^{\text{Hermite}}(\mathbf{R}) = \tilde{A}_0 H_{n_x}(\frac{2x}{L_x}) H_{n_y}(\frac{2y}{L_y}) H_{n_z}(\frac{2z}{L_z})$. These functions are similar to the envelopes of the electronic basis states in the QD. Again, we can decompose the integral into one-dimensional problems. In addition to the above-mentioned selection rules, we get

- (3) $a_{\text{elec}}^\alpha + a_{\text{hole}}^\alpha \geq n_\alpha$.

Therewith, for example the transitions between the envelopes $a_{\text{hole}}^\alpha = n_\alpha$ and $a_{\text{elec}}^\alpha = 0$ are just accessible by the light field $\sim H_{n_\alpha}(\frac{2\alpha}{L_\alpha})$, respectively for each n_α . Thus any superposition of Hermite polynomials would lead to less restrictive selection rules regarding those states. In particular, it is not possible to find light fields which just address one transition or increase the selectivity to $\Delta a^\alpha = n_\alpha$. However, $\tilde{A}^{\text{Hermite}}$ includes unrealistically small radial variations on the order of the QD size. Thus it is just discussed in this theoretical paragraph.

Cylindrical multipole modes. For the cylindrical multipole modes discussed in the main part of the paper, the selection rules can be deduced from the above findings via an expansion into Hermite polynomials

$$r^n \cos(n\varphi) = \sum_{m=0}^{\frac{n}{2}} (-1)^m \binom{n}{2m} H_{n-2m}(x) H_{2m}(y),$$

$$r^n \cos\left(n\varphi - \frac{\pi}{2}\right) = \sum_{m=1}^{\frac{n+1}{2}} (-1)^{m-1} \binom{n}{2m-1} \times H_{n-2m+1}(x) H_{2m-1}(y). \quad (\text{B1})$$

The resulting selection rules (see Sec. III) are similar to those of single Hermite polynomials, but lack the independent validity in each direction.

APPENDIX C: WHICH SELECTION RULES ARE BROKEN BY WHICH INTERACTION?

It is instructive to understand, for each interaction, which selection rule it breaks or preserves.

CDI. CDI has no effect on spins and thus no effect on spin selection rules. However, it causes mixtures between envelopes: The two electron-hole pair basis states described by a_{elec}^α and a_{hole}^α as well as $\tilde{a}_{\text{elec}}^\alpha$ and $\tilde{a}_{\text{hole}}^\alpha$ get mixed, if $(a_{\text{elec}}^\alpha + a_{\text{hole}}^\alpha) - (\tilde{a}_{\text{elec}}^\alpha + \tilde{a}_{\text{hole}}^\alpha) \in \{0, 2, 4, \dots\}$. This breaks the third envelope selection rule and reduces the second envelope selection rule to the statement that “the parity of Δa^z has to be even” (see Sec. III). In consequence, for example weak $d_{xx} \rightarrow s$ transitions become allowed already for plane-wave-like light ($n = 0$).

$\beta \neq 1$. Different confinement lengths ($\beta \neq 1$) lead to nonorthogonal sets of envelope basis functions for electrons and holes. Therefore the optical transition integrals $M_{a_1, a_2; b_1, b_2}(\tilde{A})$ [Eq. (6)] result in more nonvanishing transitions, effectively leading to the same reduction of the second selection rule as CDI. The third envelope selection rule is not touched by $\beta \neq 1$.

SRE. SRE does not mix different envelopes; thus no envelope selection rule is affected. The spin basis states are chosen in a suitable basis for SRE; thus spin selection rules are also not affected.

VBM. If we just treat the VBM-induced mixtures between envelopes, which follow the symmetry $\sum_\alpha (a_{\text{elec}}^\alpha + a_{\text{hole}}^\alpha) - (\tilde{a}_{\text{elec}}^\alpha + \tilde{a}_{\text{hole}}^\alpha) \in \{0, 2, 4, \dots\}$, we see that the direction of excitation is not important anymore and the pure envelope selection rules are reduced to modulo($\Delta a^x + \Delta a^y + \Delta a^z, 2$) = modulo($n, 2$). Thus transitions with $\Delta a^z \neq 0$ become allowed

and transitions previously just allowed with high n become allowed already with lower n , like $d_{xy} \rightarrow s$ in $n = 0$. However, with VBM the coupling between two envelopes is always accompanied by a spin flip and the degree of freedom of spin and envelope get intermixed. Thus we should look for a combined spin and envelope selection rule. Such a rule can be deduced from Fig. 4.

APPENDIX D: BREAKING OF REFLECTION SYMMETRY

Our QD model preserves a threefold reflection symmetry (thus D_{2h} symmetry), leading to eight subspaces (see Fig. 4) which are separately addressable by light fields of the corresponding parity (see Fig. 4). In realistic QDs, this symmetry is broken, with the consequence that states of different subspaces mix. For a broken reflection symmetry in the z direction, those subspaces with different parity in the z direction mix, here $(*, *, E)$ and $(*, *, O)$ (or $B_{2u} \leftrightarrow B_{3g}/B_{3u} \leftrightarrow B_{2g}/A_u \leftrightarrow B_{1g}/B_{1u} \leftrightarrow A_g$), leading to a reduction to 4 subspaces, i.e., C_{2v} symmetry. This is similar for a broken reflection symmetry in the x and y directions. If the reflection symmetry is broken in all directions, all subspaces mix and all selection rules are broken. A quantitative description of the effect of symmetry breaking on the absorption spectra goes beyond the scope of this paper. However, for a reasonably small breaking of reflection symmetries, just small changes to the considered spectra are expected, as discussed in the following.

One possibility for a breaking of the D_{2h} symmetry is a more complex shape of the QD confinement. A typical example for a broken reflection symmetry in the z direction is a pyramidal QD (C_{2v} symmetry). This would mix the spectra of light fields with even (odd) n and x/y polarization and those with odd (even) n and z polarization. For a mixture of the spectra of equally polarized light fields and just different parities of n , we need a broken reflection symmetry in in-plane direction. Therefore one would need for example a QD with a pear shape in in-plane direction, which is a less commonly supposed geometry. In fact there are both, QDs with indications for a strongly broken [46] and well-preserved [31] C_{2v} symmetry. To estimate the influence of a broken reflection symmetry of the QD confinement, we consider a general potential $\sum_{\alpha \in \{x, y, z\}} \hbar \omega_{b, \alpha} \sum_n C_n^\alpha \left(\sqrt{\frac{m_{b, \alpha} \omega_{b, \alpha}}{2\hbar}} \alpha \right)^n$ with the coefficients C_n^α . We just study the first and second order terms with $C_2^\alpha = 1$, $C_1^\alpha = \sqrt{2} C^\alpha$, and all other $C_n^\alpha = 0$. This results in a displaced quadratic potential. When shifting the potential for electrons and holes in different directions, we break the reflection symmetry in the respective direction. To break the reflection symmetry noticeably within the absorption spectra we set $C^x = C^y = C^z = \frac{1}{4}$, corresponding to a distance between the center of the electron and hole confinement of around $\frac{1}{4} L_\alpha$ [72] in the respective direction. The resulting absorption spectra are displayed in Fig. 6 and fit well to the theoretical discussion of a broken reflection symmetry in Sec. IV. A typical effect is visible for the $(p_{\text{impl}} \rightarrow s) \epsilon_{x/y}$ transitions, which become slightly bright in the spectra of light modes with $n = 0$ and $n = 2$.

Also static electric fields E can break the reflection symmetry by the Hamiltonian $\hat{H}_{\text{electr}} = -qE \cdot \hat{r}$ with opposite

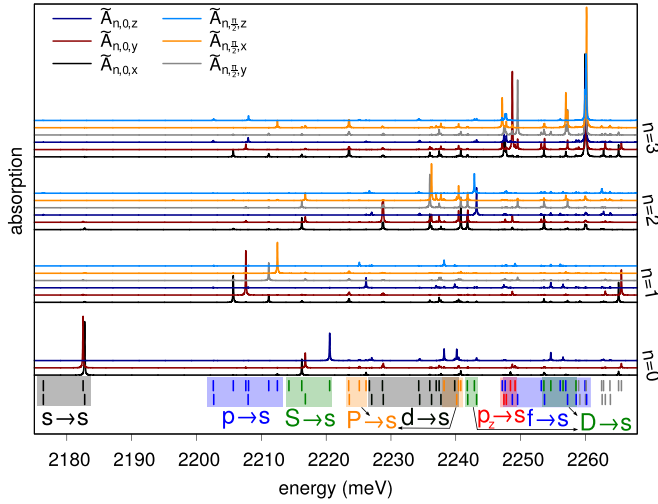


FIG. 6. Absorption spectra for a QD in our full model with broken reflection symmetry for different linear polarizations α and different rotations θ . Below, all existing exciton eigenstates are displayed in blocks labeled by the most appropriate envelope basis state. Absorption lines and states have an independent coloring.

charges q of the hole/electron. For plane-wave-like excitation and our QD parameters, we would need field strengths of

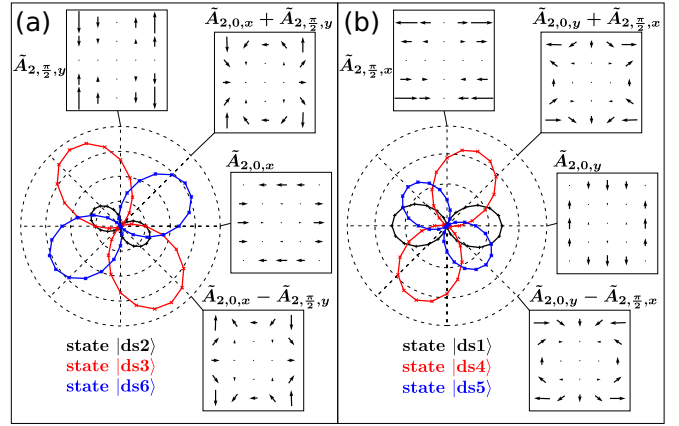


FIG. 7. Intensity of the $(d_{\text{impl}} \rightarrow s)_{\epsilon_{x/y}}$ eigenstates for different superpositions of $\tilde{A}_{2,0,x}$ and $\tilde{A}_{2,\pi/2,y}$ [$\tilde{A}_{2,0,y}$ and $\tilde{A}_{2,\pi/2,x}$] in (a) [(b)]. The insets display the corresponding field profiles.

around $5 \frac{\text{meV}}{\text{nm}}$ to get intensities of $p_x \rightarrow s$ similar to those of $d_{\text{impl}} \rightarrow s$. This could enable another way to excite for example $p \rightarrow s$ excitons by shortly activating an electric field while exciting with plane-wave-like light. The selection rules can also be broken by a reduced symmetry of the light fields.

APPENDIX E: MEASUREMENT OF $d_{\text{impl}} \rightarrow s$ EIGENSTATES

From theoretical considerations we know that the approximate eigenstates mostly consisting of $d_{\text{impl}} \rightarrow s$ are given via (from lower to higher energy)

$$\begin{aligned}
 |\text{ds1}\rangle &= \frac{1}{\sqrt{2}}[C_1|(d_{xx} \rightarrow s)\epsilon_y\rangle + \tilde{C}_1|(d_{yy} \rightarrow s)\epsilon_y\rangle] + \tilde{C}_1|(d_{xy} \rightarrow s)\epsilon_x\rangle, \\
 |\text{ds2}\rangle &= \frac{1}{\sqrt{2}}[C_2|(d_{xx} \rightarrow s)\epsilon_x\rangle + \tilde{C}_2|(d_{yy} \rightarrow s)\epsilon_x\rangle] - \tilde{C}_2|(d_{xy} \rightarrow s)\epsilon_y\rangle, \\
 |\text{ds3}\rangle &= C_3|(d_{xy} \rightarrow s)\epsilon_y\rangle - \frac{1}{\sqrt{2}}[\tilde{C}_3|(d_{xx} \rightarrow s)\epsilon_x\rangle - \tilde{C}_3|(d_{yy} \rightarrow s)\epsilon_x\rangle], \\
 |\text{ds4}\rangle &= C_4|(d_{xy} \rightarrow s)\epsilon_x\rangle + \frac{1}{\sqrt{2}}[\tilde{C}_4|(d_{xx} \rightarrow s)\epsilon_y\rangle - \tilde{C}_4|(d_{yy} \rightarrow s)\epsilon_y\rangle], \\
 |\text{ds5}\rangle &= \frac{1}{\sqrt{2}}[\tilde{C}_5|(d_{xx} \rightarrow s)\epsilon_y\rangle - C_5|(d_{yy} \rightarrow s)\epsilon_y\rangle] - \tilde{C}_5|(d_{xy} \rightarrow s)\epsilon_x\rangle, \\
 |\text{ds6}\rangle &= \frac{1}{\sqrt{2}}[\tilde{C}_6|(d_{xx} \rightarrow s)\epsilon_x\rangle - C_6|(d_{yy} \rightarrow s)\epsilon_x\rangle] + \tilde{C}_6|(d_{xy} \rightarrow s)\epsilon_y\rangle,
 \end{aligned} \tag{E1}$$

with typically $C_i > \tilde{C}_i > \tilde{C}_i$. The light modes $\tilde{A}_{2,0,\alpha} \sim (x^2 - y^2)e_\alpha$ and $\tilde{A}_{2,\pi/2,\alpha} \sim xy e_\alpha$ excite the states $(d_{xx} \rightarrow s)\epsilon_\alpha - (d_{yy} \rightarrow s)\epsilon_\alpha$ and $(d_{xy} \rightarrow s)\epsilon_\alpha$, respectively. The absorption for different real superpositions of these modes is given in Fig. 7.

With these two light modes, we can just reveal the coefficients of a 2-dimensional basis. A change from the basis states $(d_{xx} \rightarrow s)\epsilon_\alpha$ and $(d_{yy} \rightarrow s)\epsilon_\alpha$ to $(d_{xx} \rightarrow s)\epsilon_\alpha \pm (d_{yy} \rightarrow s)\epsilon_\alpha$, where $(d_{xx} \rightarrow s)\epsilon_\alpha + (d_{yy} \rightarrow s)\epsilon_\alpha$ is dark so its coefficient cannot be measured anyway, provides a well-defined 2-dimensional basis. The eigenstates obtained from the simulated measurement in Fig. 7 fit well to the theoretically predicted form of Eqs. (E1). The angle mismatch between the “measured” eigenstate and the “exact” eigenstate without higher terms is 3° – 14° . The accuracy is reduced compared to the measurement of the $p_{\text{impl}} \rightarrow s$ states, since the $d_{\text{impl}} \rightarrow s$ eigenstates have larger contributions of energetically higher basis states (more than 30%).

APPENDIX F: DIFFERENT REPRESENTATIONS OF BESSEL BEAMS

An exact solution of the Helmholtz equation is given by Bessel beams [73,74]. We discuss three equivalent representations, as listed below. For all cases, we give approximations up to a useful level. Therefore we consider $\frac{q_r}{q_z} \approx 1$ and a region around $q_r r = 0$, thus $J_n(q_r r) = \sum_{j=0}^{\infty} \frac{(-1)^j (\frac{q_r r}{2})^{2j+n}}{(j+n)! j!} \approx \frac{(q_r r)^n}{2^n n!}$ and $(q_r r)^{n+1} \ll (q_r r)^n$ [75]. Please note that the neglected terms of higher order in $q_r r$ have a safely negligible impact on the absorption spectra, since the absorption rate is even of quadratic order in the field amplitudes. One can construct standing waves by a superposition of two waves propagating in opposite directions. Thereby different local fields arise at different values of z . For small $q_z z$ we use $\cos(q_z z) \approx 1$ and $\sin(q_z z) \approx q_z z$. We use the cylindrical coordinates r , φ , and z .

(1) *Twisted light beams*. This representation is similar to a complex-valued cylindrical multipole expansion, Laguerre-Gaussian beams, so-called vortex beams or twisted light. The fields can be described by nodal planes with a normal in in-plane direction, which rotate in space and time, giving them the nickname “twisted light.” Within the paraxial limit, the indices l and σ label the orbital angular momentum and circular polarization of the mode, respectively.

Traveling waves:

$$\begin{aligned} A_{l,\sigma}(\mathbf{r}, t) &= A_0 e^{i(q_z z - \omega t)} \left[J_l(q_r r) e^{il\varphi} \frac{1}{\sqrt{2}} (\mathbf{e}_x + i\sigma \mathbf{e}_y) - \frac{i\sigma}{\sqrt{2}} \frac{q_r}{q_z} J_{l+\sigma}(q_r r) e^{i(l+\sigma)\varphi} \mathbf{e}_z \right] + \text{c.c.} \\ &\approx \begin{cases} A_0 e^{i(q_z z - \omega t)} \left[J_l(q_r r) e^{il\varphi} \frac{1}{\sqrt{2}} (\mathbf{e}_x + i\sigma \mathbf{e}_y) \right] + \text{c.c.}, & \text{for } \text{sgn}(l) = \text{sgn}(\sigma), \\ A_0 e^{i(q_z z - \omega t)} \left[-\frac{i\sigma}{\sqrt{2}} \frac{q_r}{q_z} J_{l+\sigma}(q_r r) e^{i(l+\sigma)\varphi} \mathbf{e}_z \right] + \text{c.c.}, & \text{for } \text{sgn}(l) \neq \text{sgn}(\sigma). \end{cases} \end{aligned} \quad (\text{F1})$$

(2) *Radially and azimuthally polarized beams*. This representation is somewhere between the complex- and real-valued cylindrical multipole expansions. Radially and azimuthally polarized beams are exemplary realizations. These modes become interesting for QDs with cylindrical symmetry or fields with a strong component polarized in propagation direction (here the z direction). Corresponding standing waves are given in Eqs. (F3).

Traveling waves:

$$\begin{aligned} \mathbf{A}_{n,\theta}^{\text{xy}}(\mathbf{r}, t) &= \begin{cases} \frac{1}{\sqrt{2}} [\mathbf{A}_{n,1}(\mathbf{r}, t) + (-1)^n \mathbf{A}_{-n,-1}(\mathbf{r}, t)], & \text{for } \theta = 0, \\ \frac{-i}{\sqrt{2}} [\mathbf{A}_{n,1}(\mathbf{r}, t) - (-1)^n \mathbf{A}_{-n,-1}(\mathbf{r}, t)], & \text{for } \theta = \frac{\pi}{2}, \end{cases} \\ &= A_0 e^{i(q_z z - \omega t)} \left\{ J_n(q_r r) [\cos(n\varphi - \theta) \mathbf{e}_x - \sin(n\varphi - \theta) \mathbf{e}_y] - i \frac{q_r}{q_z} J_{n+1}(q_r r) \cos[(n+1)\varphi - \theta] \mathbf{e}_z \right\} + \text{c.c.} \\ &\approx A_0 2 \cos(q_z z - \omega t) \frac{q_r^n r^n}{2^n n!} [\cos(n\varphi - \theta) \mathbf{e}_x - \sin(n\varphi - \theta) \mathbf{e}_y], \\ \mathbf{A}_{n,\theta}^z(\mathbf{r}, t) &= \begin{cases} \frac{1}{\sqrt{2}} [\mathbf{A}_{n+1,-1}(\mathbf{r}, t) + (-1)^{n+1} \mathbf{A}_{-(n+1),1}(\mathbf{r}, t)], & \text{for } \theta = 0, \\ \frac{-i}{\sqrt{2}} [\mathbf{A}_{n+1,-1}(\mathbf{r}, t) - (-1)^{n+1} \mathbf{A}_{-(n+1),1}(\mathbf{r}, t)], & \text{for } \theta = \frac{\pi}{2}, \end{cases} \\ &= A_0 e^{i(q_z z - \omega t)} \left[J_{n+1}(q_r r) \{ \cos[(n+1)\varphi - \theta] \mathbf{e}_x + \sin[(n+1)\varphi - \theta] \mathbf{e}_y \} + i \frac{q_r}{q_z} J_n(q_r r) \cos(n\varphi - \theta) \mathbf{e}_z \right] + \text{c.c.} \\ &\approx \begin{cases} A_0 2 \cos(q_z z - \omega t) \frac{q_r r}{2} [\cos(\varphi - \theta) \mathbf{e}_x + \sin(\varphi - \theta) \mathbf{e}_y], & \text{for } n = 0, \theta = \frac{\pi}{2}, \\ A_0 2 \sin(q_z z - \omega t) \frac{q_r}{q_z} \frac{q_r^n r^n}{2^n n!} \cos(n\varphi - \theta) \mathbf{e}_z, & \text{else.} \end{cases} \end{aligned} \quad (\text{F2})$$

Standing waves:

$$\begin{aligned} \check{\mathbf{A}}_{n,\theta}^{\text{xy}}(\mathbf{r}, t) &= A_0 2 \cos(\omega t) \left\{ \cos(q_z z) J_n(q_r r) [\cos(n\varphi - \theta) \mathbf{e}_x - \sin(n\varphi - \theta) \mathbf{e}_y] + \sin(q_z z) \frac{q_r}{q_z} J_{n+1}(q_r r) \cos[(n+1)\varphi - \theta] \mathbf{e}_z \right\} \\ &\approx \frac{2A_0}{2^n n!} \cos(\omega t) \left\{ q_r^n r^n [\cos(n\varphi - \theta) \mathbf{e}_x - \sin(n\varphi - \theta) \mathbf{e}_y] + \frac{1}{2n(n+1)} \frac{nz}{r} q_r^{n+2} r^{n+2} \cos[(n+1)\varphi - \theta] \mathbf{e}_z \right\}, \\ \check{\mathbf{A}}_{n,\theta}^z(\mathbf{r}, t) &= A_0 2 \cos(\omega t) \left[\cos(q_z z) J_{n+1}(q_r r) \{ \cos[(n+1)\varphi - \theta] \mathbf{e}_x + \sin[(n+1)\varphi - \theta] \mathbf{e}_y \} - \sin(q_z z) \frac{q_r}{q_z} J_n(q_r r) \cos(n\varphi - \theta) \mathbf{e}_z \right] \\ &\stackrel{z \approx 0}{\approx} \frac{2A_0}{2^{n+1}(n+1)!} \cos(\omega t) \left[q_r^{n+1} r^{n+1} \{ \cos[(n+1)\varphi - \theta] \mathbf{e}_x + \sin[(n+1)\varphi - \theta] \mathbf{e}_y \} \right. \\ &\quad \left. - 2 \frac{(n+1)z}{r} q_r^{n+1} r^{n+1} \cos(n\varphi - \theta) \mathbf{e}_z \right] \end{aligned}$$

or

$$\begin{aligned} & \underbrace{z \approx -\frac{\pi}{2q_z}}_{\approx} \frac{q_r}{q_z} \frac{2A_0}{2^n n!} \cos(\omega t) \left[\frac{1}{2(n+1)} \frac{1}{\left(\frac{q_z}{r}\right)^2} \frac{z + \frac{\pi}{2q_z}}{r} (q_r r)^{n+2} \{\cos[(n+1)\varphi - \theta] \mathbf{e}_x + \sin[(n+1)\varphi - \theta] \mathbf{e}_y\} \right. \\ & \quad \left. + (q_r r)^n \cos(n\varphi - \theta) \mathbf{e}_z \right] \\ & \approx \frac{q_r}{q_z} 2A_0 \cos(\omega t) \frac{(q_r r)^n}{2^n n!} \cos(n\varphi - \theta) \mathbf{e}_z. \end{aligned} \quad (\text{F3})$$

(3) *Real-valued cylindrical multipole modes.* This representation is similar to a real-valued cylindrical multipole expansion, as used throughout this paper. Compared to the complex-valued expansion, the nodal planes of the field have a fixed orientation in space and time.

Traveling waves:

$$\begin{aligned} \mathbf{A}_{n,\theta}^x(\mathbf{r}, t) &= \begin{cases} \mathbf{A}_{0,0}^{xy}(\mathbf{r}, t), & \text{for } n=0, \theta=0, \\ \frac{1}{2}[\mathbf{A}_{n,\theta}^{xy}(\mathbf{r}, t) + \mathbf{A}_{n-1,\theta}^z(\mathbf{r}, t)], & \text{for } n \geq 1, \end{cases} \\ &= A_0 e^{i(q_z z - \omega t)} \left[J_n(q_r r) \cos(n\varphi - \theta) \mathbf{e}_x - \frac{i}{2} \frac{q_r}{q_z} \{J_{n+1}(q_r r) \cos[(n+1)\varphi - \theta] - J_{n-1}(q_r r) \cos[(n-1)\varphi - \theta]\} \mathbf{e}_z \right] + \text{c.c.}, \\ \mathbf{A}_{n,\theta}^y(\mathbf{r}, t) &= \begin{cases} \mathbf{A}_{0,\frac{\pi}{2}}^{xy}(\mathbf{r}, t), & \text{for } n=0, \theta=0, \\ \frac{1}{2}[\mathbf{A}_{n,\frac{\pi}{2}}^{xy}(\mathbf{r}, t) - \mathbf{A}_{n-1,\frac{\pi}{2}}^z(\mathbf{r}, t)], & \text{for } n \geq 1, \theta=0, \\ \frac{-1}{2}[\mathbf{A}_{n,0}^{xy}(\mathbf{r}, t) - \mathbf{A}_{n-1,0}^z(\mathbf{r}, t)], & \text{for } n \geq 1, \theta=\frac{\pi}{2}, \end{cases} \\ &= A_0 e^{i(q_z z - \omega t)} \left[J_n(q_r r) \cos(n\varphi - \theta) \mathbf{e}_y - \frac{i}{2} \frac{q_r}{q_z} \{J_{n+1}(q_r r) \sin[(n+1)\varphi - \theta] + J_{n-1}(q_r r) \sin[(n-1)\varphi - \theta]\} \mathbf{e}_z \right] + \text{c.c.} \end{aligned} \quad (\text{F4})$$

Standing waves:

$$\begin{aligned} \check{\mathbf{A}}_{n,\theta}^x(\mathbf{r}, t) &= A_0 2 \cos(\omega t) \\ & \times \left[\cos(q_z z) J_n(q_r r) \cos(n\varphi - \theta) \mathbf{e}_x + \frac{1}{2} \sin(q_z z) \frac{q_r}{q_z} \{J_{n+1}(q_r r) \cos[(n+1)\varphi - \theta] - J_{n-1}(q_r r) \cos[(n-1)\varphi - \theta]\} \mathbf{e}_z \right] \\ & \approx \frac{2A_0}{2^n n!} \cos(\omega t) \left\{ q_r^n r^n \cos(n\varphi - \theta) \mathbf{e}_x - \frac{nz}{r} q_r^n r^n \cos[(n-1)\varphi - \theta] \mathbf{e}_z \right\}, \check{\mathbf{A}}_{n,\theta}^y(\mathbf{r}, t) = A_0 2 \cos(\omega t) \\ & \times \left[\cos(q_z z) J_n(q_r r) \cos(n\varphi - \theta) \mathbf{e}_y + \frac{1}{2} \sin(q_z z) \frac{q_r}{q_z} \{J_{n+1}(q_r r) \sin[(n+1)\varphi - \theta] + J_{n-1}(q_r r) \sin[(n-1)\varphi - \theta]\} \mathbf{e}_z \right] \\ & \approx \frac{2A_0}{2^n n!} \cos(\omega t) \left\{ q_r^n r^n \cos(n\varphi - \theta) \mathbf{e}_y + \frac{nz}{r} q_r^n r^n \sin[(n-1)\varphi - \theta] \mathbf{e}_z \right\}. \end{aligned} \quad (\text{F5})$$

-
- [1] K. Shibata, S. Tojo, and D. Bloch, Excitation enhancement in electric multipole transitions near a nanoedge, *Opt. Express* **25**, 9476 (2017).
- [2] M. L. M. Balistreri, J. P. Korterik, L. Kuipers, and N. F. van Hulst, Local Observations of Phase Singularities in Optical Fields in Waveguide Structures, *Phys. Rev. Lett.* **85**, 294 (2000).
- [3] M. Abashin, P. Tortora, I. Märki, U. Levy, W. Nakagawa, L. Vaccaro, H. P. Herzig, and Y. Fainman, Near-field characterization of propagating optical modes in photonic crystal waveguides, *Opt. Express* **14**, 1643 (2006).
- [4] G. Cui, J. M. Hannigan, R. Loeckenhoff, F. M. Matinaga, M. G. Raymer, S. Bhongale, M. Holland, S. Mosor, S. Chatterjee, H. M. Gibbs *et al.*, A hemispherical, high-solid-angle optical micro-cavity for cavity-QED studies, *Opt. Express* **14**, 2289 (2006).
- [5] X. Cai, J. Wang, M. J. Strain, B. Johnson-Morris, J. Zhu, M. Sorel, J. L. O'Brien, M. G. Thompson, and S. Yu, Integrated compact optical vortex beam emitters, *Science* **338**, 363 (2012).
- [6] A. G. Curto, T. H. Taminiau, G. Volpe, M. P. Kreuzer, R. Quidant, and Niek F. van Hulst, Multipolar radiation of quantum emitters with nanowire optical antennas, *Nat. Commun.* **4**, 1750 (2013).
- [7] C. T. Schmiegelow, J. Schulz, H. Kaufmann, T. Ruster, U. G. Poschinger, and F. Schmidt-Kaler, Transfer of optical orbital angular momentum to a bound electron, *Nat. Commun.* **7**, 12998 (2016).
- [8] R. M. Kerber, J. M. Fitzgerald, D. E. Reiter, S. S. Oh, and O. Hess, Reading the orbital angular momentum of light using plasmonic nanoantennas, *ACS Photonics* **4**, 891 (2017).

- [9] G. F. Quinteiro, D. E. Reiter, and T. Kuhn, Formulation of the twisted-light-matter interaction at the phase singularity: The twisted-light gauge, *Phys. Rev. A* **91**, 033808 (2015).
- [10] G. F. Quinteiro, C. T. Schmiegelow, D. E. Reiter, and T. Kuhn, Reexamination of Bessel beams: A generalized scheme to derive optical vortices, *Phys. Rev. A* **99**, 023845 (2019).
- [11] B. K. Singh, H. Nagar, Y. Roichman, and A. Arie, Particle manipulation beyond the diffraction limit using structured super-oscillating light beams, *Light Sci. Appl.* **6**, e17050 (2017).
- [12] F. M. Huang and N. I. Zheludev, Super-resolution without evanescent waves, *Nano Lett.* **9**, 1249 (2009).
- [13] A. Mair, A. Vaziri, G. Weihs, and A. Zeilinger, Entanglement of the orbital angular momentum states of photons, *Nature (London)* **412**, 313 (2001).
- [14] G. Molina-Terriza, J. P. Torres, and L. Torner, Twisted photons, *Nat. Phys.* **3**, 305 (2007).
- [15] A. Vaziri, G. Weihs, and A. Zeilinger, Experimental Two-photon, Three-Dimensional Entanglement for Quantum Communication, *Phys. Rev. Lett.* **89**, 240401 (2002).
- [16] J. T. Barreiro, T. C. Wei, and P. G. Kwiat, Beating the channel capacity limit for linear photonic superdense coding, *Nat. Phys.* **4**, 282 (2008).
- [17] E. Nagali, L. Sansoni, F. Sciarrino, F. De Martini, L. Marrucci, B. Piccirillo, E. Karimi, and E. Santamato, Optimal quantum cloning of orbital angular momentum photon qubits through Hong-Ou-Mandel coalescence, *Nat. Photonics* **3**, 720 (2009).
- [18] J. Wang, J. Y. Yang, I. M. Fazal, N. Ahmed, Y. Yan, H. Huang, Y. Ren, Y. Yue, S. Dolinar, M. Tur *et al.*, Terabit free-space data transmission employing orbital angular momentum multiplexing, *Nat. Photonics* **6**, 488 (2012).
- [19] N. Bozinovic, Y. Yue, Y. Ren, M. Tur, P. Kristensen, H. Huang, A. E. Willner, and S. Ramachandran, Terabit-scale orbital angular momentum mode division multiplexing in fibers, *Science* **340**, 1545 (2013).
- [20] D. J. Richardson, J. M. Fini, and L. E. Nelson, Space-division multiplexing in optical fibres, *Nat. Photonics* **7**, 354 (2013).
- [21] S. L. Portalupi, M. Jetter, and P. Michler, InAs quantum dots grown on metamorphic buffers as non-classical light sources at telecom C-band: A review, *Semicond. Sci. Technol.* **34**, 053001 (2019).
- [22] Ł. Dusanowski, S. H. Kwon, C. Schneider, and S. Höfling, Near-Unity Indistinguishability Single Photon Source for Large-Scale Integrated Quantum Optics, *Phys. Rev. Lett.* **122**, 173602 (2019).
- [23] D. E. Reiter, T. Kuhn, and V. M. Axt, Distinctive characteristics of carrier-phonon interactions in optically driven semiconductor quantum dots, *Adv. Phys. X* **4**, 1655478 (2019).
- [24] R. Trivedi, Fischer K. A., J. Vučković, and K. Müller, Generation of non-classical light using semiconductor quantum dots, *Adv. Quantum Technol.* **3**, 1900007 (2020).
- [25] M. Kneissl, A. Knorr, S. Reitzenstein, and A. Hoffmann, *Semiconductor Nanophotonics: Materials, Models, and Devices* (Springer International Publishing, 2020).
- [26] T. Kupko, M. von Helversen, L. Rickert, J.-H. Schulze, A. Strittmatter, M. Gschrey, S. Rodt, S. Reitzenstein, and T. Heindel, Tools for the performance optimization of single-photon quantum key distribution, *npj Quantum Inf.* **6**, 29 (2020).
- [27] P. Michler, *Quantum Dots for Quantum Information Technologies* (Springer International Publishing, 2017).
- [28] D. Huber, M. Reindl, J. Aberl, A. Rastelli, and R. Trotta, Semiconductor quantum dots as an ideal source of polarization-entangled photon pairs on-demand: A review, *J. Opt.* **20**, 073002 (2018).
- [29] A. J. Ramsay, A review of the coherent optical control of the exciton and spin states of semiconductor quantum dots, *Semicond. Sci. Technol.* **25**, 103001 (2010).
- [30] R. J. Warburton, Single spins in self-assembled quantum dots, *Nat. Mater.* **12**, 483 (2013).
- [31] C. Hinz, P. Gumbsheimer, C. Traum, M. Holtkemper, B. Bauer, J. Haase, S. Mahapatra, A. Frey, K. Brunner, D. E. Reiter, T. Kuhn, D. V. Seletskiy, and A. Leitenstorfer, Charge and spin control of ultrafast electron and hole dynamics in single CdSe/ZnSe quantum dots, *Phys. Rev. B* **97**, 045302 (2018).
- [32] P. Hawrylak, Excitonic artificial atoms: Engineering optical properties of quantum dots, *Phys. Rev. B* **60**, 5597 (1999).
- [33] I. A. Akimov, A. Hundt, T. Flissikowski, and F. Henneberger, Fine structure of the trion triplet state in a single self-assembled semiconductor quantum dot, *Appl. Phys. Lett.* **81**, 4730 (2002).
- [34] D. Chithrani, M. Korkusinski, S. J. Cheng, P. Hawrylak, R. L. Williams, J. Lefebvre, P. J. Poole, and G. C. Aers, Electronic structure of the p-shell in single, site-selected InAs/InP quantum dots, *Physica E* **26**, 322 (2005).
- [35] A. Babinski, M. Potemski, S. Raymond, J. Lapointe, and Z. R. Wasilewski, Emission from a highly excited single InAs-GaAs quantum dot in magnetic fields: An excitonic Fock-Darwin diagram, *Phys. Rev. B* **74**, 155301 (2006).
- [36] Y. Arashida, Y. Ogawa, and F. Minami, Four-photon cascade from quadexcitons in a single GaAs quantum dot, *Phys. Rev. B* **84**, 125309 (2011).
- [37] K. Kukliński, K. Fronc, M. Wiater, P. Wojnar, P. Rutkowski, V. Voliotis, R. Grousson, G. Karczewski, J. Kossut, T. Wojtowicz *et al.*, Tuning the inter-shell splitting in self-assembled CdTe quantum dots, *Appl. Phys. Lett.* **99**, 141906 (2011).
- [38] M. Molas, K. Gołasa, M. Furman, J. Lapointe, Z. R. Wasilewski, M. Potemski, and A. Babiński, The fine structure of a triexciton in single InAs/GaAs quantum dots, *Acta Phys. Pol. A* **122**, 991 (2012).
- [39] B. Pietka, J. Suffczyński, M. Goryca, T. Kazimierzczuk, A. Golnik, P. Kossacki, A. Wymolek, J. A. Gaj, R. Stepniowski, and M. Potemski, Photon correlation studies of charge variation in a single GaAlAs quantum dot, *Phys. Rev. B* **87**, 035310 (2013).
- [40] M. R. Molas, A. A. L. Nicolet, A. Babiński, and M. Potemski, Quadexciton cascade and fine-structure splitting of the triexciton in a single quantum dot, *Europhys. Lett.* **113**, 17004 (2016).
- [41] I. Schwartz, E. R. Schmidgall, L. Gantz, D. Cogan, E. Bordo, Y. Don, M. Zielinski, and D. Gershoni, Deterministic Writing and Control of the Dark Exciton Spin Using Single Short Optical Pulses, *Phys. Rev. X* **5**, 011009 (2015).
- [42] C. Traum, P. Henzler, D. Nabben, M. Holtkemper, D. E. Reiter, T. Kuhn, D. V. Seletskiy, and A. Leitenstorfer, Ultrafast analysis and control of sub-nanosecond intraband coherence in single CdSe/ZnSe quantum dots, in *CLEO: QELS Fundamental Science* (Optical Society of America, San Jose, California, 2019), pp. FM3D-4.
- [43] H. Htoon, D. Kulik, O. Baklenov, A. L. Holmes Jr., T. Takagahara, and C. K. Shih, Carrier relaxation and quantum

- decoherence of excited states in self-assembled quantum dots, *Phys. Rev. B* **63**, 241303(R) (2001).
- [44] J. Huneke, I. D'Amico, P. Machnikowski, T. Thomay, R. Bratschitsch, A. Leitenstorfer, and T. Kuhn, Role of Coulomb correlations for femtosecond pump-probe signals obtained from a single quantum dot, *Phys. Rev. B* **84**, 115320 (2011).
- [45] D. Gammon, E. S. Snow, B. V. Shanabrook, D. S. Katzer, and D. Park, Fine Structure Splitting in the Optical Spectra of Single GaAs Quantum Dots, *Phys. Rev. Lett.* **76**, 3005 (1996).
- [46] Y. Benny, Y. Kodriano, E. Poem, D. Gershoni, T. A. Truong, and P. M. Petroff, Excitation spectroscopy of single quantum dots at tunable positive, neutral, and negative charge states, *Phys. Rev. B* **86**, 085306 (2012).
- [47] M. R. Molas, A. Wójs, A. A. L. Nicolet, A. Babiński, and M. Potemski, Energy spectrum of confined positively charged excitons in single quantum dots, *Phys. Rev. B* **94**, 235416 (2016).
- [48] M. Holtkemper, D. E. Reiter, and T. Kuhn, Influence of the quantum dot geometry on p-shell transitions in differently charged quantum dots, *Phys. Rev. B* **97**, 075308 (2018).
- [49] J. R. Zurita-Sánchez and L. Novotny, Multipolar interband absorption in a semiconductor quantum dot. I. Electric quadrupole enhancement, *J. Opt. Soc. Am. B* **19**, 1355 (2002).
- [50] J. R. Zurita-Sánchez and L. Novotny, Multipolar interband absorption in a semiconductor quantum dot. II. Magnetic dipole enhancement, *J. Opt. Soc. Am. B* **19**, 2722 (2002).
- [51] G. F. Quinteiro and P. I. Tamborenea, Electronic transitions in disk-shaped quantum dots induced by twisted light, *Phys. Rev. B* **79**, 155450 (2009).
- [52] T. Maltezopoulos, A. Bolz, C. Meyer, C. Heyn, W. Hansen, M. Morgenstern, and R. Wiesendanger, Wave-Function Mapping of InAs Quantum Dots by Scanning Tunneling Spectroscopy, *Phys. Rev. Lett.* **91**, 196804 (2003).
- [53] E. E. Vdovin, A. Levin, A. Patane, L. Eaves, P. C. Main, Y. N. Khanin, Y. V. Dubrovskii, M. Henini, and G. Hill, Imaging the electron wave function in self-assembled quantum dots, *Science* **290**, 122 (2000).
- [54] A. I. Ekimov, I. A. Kudryavtsev, A. L. Efros, T. V. Yazeva, F. Hache, M. C. Schanne-Klein, A. V. Rodina, D. Ricard, and C. Flytzanis, Absorption and intensity-dependent photoluminescence measurements on CdSe quantum dots: Assignment of the first electronic transitions, *J. Opt. Soc. Am. B* **10**, 100 (1993).
- [55] U. E. H. Laheld and G. T. Einevoll, Excitons in CdSe quantum dots, *Phys. Rev. B* **55**, 5184 (1997).
- [56] M. E. Ware, A. S. Bracker, E. Stinaff, D. Gammon, D. Gershoni, and V. L. Korenev, Polarization spectroscopy of positive and negative trions in an InAs quantum dot, *Physica E* **26**, 55 (2005).
- [57] Y. Benny, Y. Kodriano, E. Poem, S. Khatsevitch, D. Gershoni, and P. M. Petroff, Two-photon photoluminescence excitation spectroscopy of single quantum dots, *Phys. Rev. B* **84**, 075473 (2011).
- [58] V. Jovanov, S. Kapfinger, M. Bichler, G. Abstreiter, and J. J. Finley, Direct observation of metastable hot trions in an individual quantum dot, *Phys. Rev. B* **84**, 235321 (2011).
- [59] The neglected terms $\partial_{R_\alpha} \tilde{\mathbf{A}}(\mathbf{R}) \cdot r_\alpha \hat{\mathbf{p}}$ are around a factor $\frac{r}{R}$ smaller, than the term $\tilde{\mathbf{A}}(\mathbf{R}) \cdot \hat{\mathbf{p}}$. Within the integration to obtain the matrix elements, the factor $\frac{r}{R}$ can be estimated by $\frac{r_{uc}}{R_{QD}}$ with the dimension of the unit cell r_{uc} and the dimension of the QD R_{QD} . Within absorption rates, this factor is even squared.
- [60] G. Bastard, *Wave Mechanics Applied to Semiconductor Heterostructures* (John Wiley and Sons, New York, 1990).
- [61] M. Holtkemper, G. F. Quinteiro, D. E. Reiter, and T. Kuhn, Dark exciton preparation in a quantum dot by a longitudinal light field tuned to higher exciton states, [arXiv:2003.03205](https://arxiv.org/abs/2003.03205).
- [62] Equivalently, one could understand a_m and $\sum_{n=1}^N \alpha_{m,n} c_n^*$ as the coefficients of two complex vectors, whose scalar product is maximal when they are parallel.
- [63] Different values for α_{11} and α_{22} arise, since we adjusted p_x and p_y to the QD elongation. We expect similar results and accuracy for nonadjusted basis states. Just the error caused by the contributions |rest – bright) is assumed to rise slightly.
- [64] $\frac{q_x}{q_z} = 1$ is a realistic value, as shown in Refs. [76,77].
- [65] S. Ninomiya and S. Adachi, Optical properties of cubic and hexagonal CdSe, *J. Appl. Phys.* **78**, 4681 (1995).
- [66] G. F. Quinteiro, A. O. Lucero, and P. I. Tamborenea, Electronic transitions in quantum dots and rings induced by inhomogeneous off-centered light beams, *J. Phys.: Condens. Matter* **22**, 505802 (2010).
- [67] J. Durnin, J. J. Miceli, and J. H. Eberly, Diffraction-Free Beams, *Phys. Rev. Lett.* **58**, 1499 (1987).
- [68] M. Woerdemann, C. Alpmann, M. Esseling, and C. Denz, Advanced optical trapping by complex beam shaping, *Laser Photonics Rev.* **7**, 839 (2013).
- [69] M. Ettore, S. C. Pavone, M. Casaletti, and M. Albani, Experimental validation of Bessel beam generation using an inward Hankel aperture distribution, *IEEE Trans. Antennas Propag.* **63**, 2539 (2015).
- [70] C. Schneider, P. Gold, S. Reitzenstein, S. Hoefling, and M. Kamp, Quantum dot micropillar cavities with quality factors exceeding 250,000, *Appl. Phys. B* **122**, 19 (2016).
- [71] J. P. Reithmaier, G. Şek, A. Löffler, C. Hofmann, S. Kuhn, S. Reitzenstein, L. V. Keldysh, V. D. Kulakovskii, T. L. Reinecke, and A. Forchel, Strong coupling in a single quantum dot-semiconductor microcavity system, *Nature (London)* **432**, 197 (2004).
- [72] This is exact for $\beta = 1$.
- [73] K. Volke-Sepulveda, V. Garcés-Chávez, S. Chávez-Cerda, J. Arlt, and K. Dholakia, Orbital angular momentum of a high-order Bessel light beam, *J. Opt. B* **4**, S82 (2002).
- [74] G. F. Quinteiro and T. Kuhn, Light-hole transitions in quantum dots: Realizing full control by highly focused optical-vortex beams, *Phys. Rev. B* **90**, 115401 (2014).
- [75] $q_r R_{QD} \approx 0.06$, as discussed in Sec. VIA.
- [76] W. Chen and Q. Zhan, Realization of an evanescent Bessel beam via surface plasmon interference excited by a radially polarized beam, *Opt. Lett.* **34**, 722 (2009).
- [77] H. Huang, Q. Li, J. Fu, J. Wu, F. Lin, and X. Wu, Efficient sub-wavelength focusing of light with a long focal depth, *Nanoscale* **7**, 16504 (2015).